Physics – Uspekhi **68** (9) 905 – 922 (2025)

INSTRUMENTS AND METHODS OF INVESTIGATION PACS numbers: 06.30.Ft, 07.85.Qe, **42.55. – f**, 61.05.C–, 61.05.cj

Pumping and X-ray probing technique

V.V. Lider

DOI: https://doi.org/10.3367/UFNe.2025.06.039943

Contents

Abstract. The principles and capabilities of the time-resolved pumping and X-ray probing method are outlined. Pumping methods and probing features involving different pulsed X-ray sources (laboratory, synchrotron, free-electron lasers) are considered. Methods for improving time resolution are discussed. Also given are examples of applying the method to study a wide range of objects using X-ray microscopy, X-ray Laue diffraction, small- and large-angle scattering, absorption, and photoelectron spectroscopy.

Keywords: pulsed X-ray sources, time resolution, synchrotrons, free-electron lasers, diffraction, X-ray scattering, absorption spectroscopy

1. Introduction

Many processes in Nature occur on very short time scales, including the motion of atoms during chemical reactions, molecular vibrations, the absorption and emission of photons, and many scattering effects. Electron motions are the fastest processes in the femtosecond (fs) and subfemtosecond regimes, optical and acoustic phonons (lattice vibrations) occur on the picosecond (ps) time scale, atomic motions and molecular vibrations occur on the subpicosecond time scale, while heat diffusion and heat transfer in crystalline solids occur more slowly. Macroscopic transformations in crystals, such as the dynamics of domains and domain walls in ferroic crystals (polarization switching in ferroelectrics) and the propagation of macroscopic elastic deformations, are prevalent in the microsecond (μs) to millisecond (ms) range; this time scale also corresponds to the lifetime of molecular metastable states [1–3]. To solve current problems in biophysics and solid-state physics requires covering such a broad time range. Therefore, a method was developed that uses different X-ray radiation sources, which in the English-language literature is called 'pump–probe' [4, 5].

Typically, the measurement technique involves the joint alignment of a pump pulse (e.g., a pulsed laser) on a sample, which triggers the process under study, and a pulsed X-ray beam, and timing the two pulses with an adjustable time delay Δt. Varying the time delay of the corresponding scattered or absorbed X-ray signal allows direct monitoring of the induced structural evolution of the sample in relation to the time delay [3].

Two components are critical to the successful performance of time-resolved X-ray experiments: reaction initiation and a pulsed X-ray source [6]. This review discusses both of these components.

2. Pump–probe method

The common physical principle of the methods for studying transient photoprocesses in different materials is as follows: a powerful pulse of pump radiation transfers the substance into a nonstationary state, in which its spectral properties differ from those in the unexcited state. After a certain characteristic time, the excitation relaxes and it returns to the initial state (reversible process) or passes into a new state (irreversible process). Completely reversible processes can be initiated repeatedly with a very high repetition rate and studied stroboscopically, whereas irreversible processes can be studied only once with a given crystalline sample [4, 7].

The reaction in the sample is triggered at $t = 0$ (pump) and the diffraction pattern (probe) is collected after a well-defined time delay Δt_1. It is necessary to have a sufficient number of patterns to obtain a good signal-to-background ratio, from which conformational changes in the sample can be determined for a time delay Δt_1 after the reaction is initiated. The

V.V. Lider
A.V. Shubnikov Institute of Crystallography
of the Kurchatov Complex Crystallography and Photonics
of the NRC Kurchatov Institute
Leninskii prosp. 59, 119333 Moscow, Russian Federation
E-mail: vallider@yandex.ru, lider@ms.crys.ras.ru

Received 4 April 2024, revised 5 June 2025
Uspekhi Fizicheskikh Nauk **195** (9) 962 – 981 (2025)
Translated by E.N. Ragozin

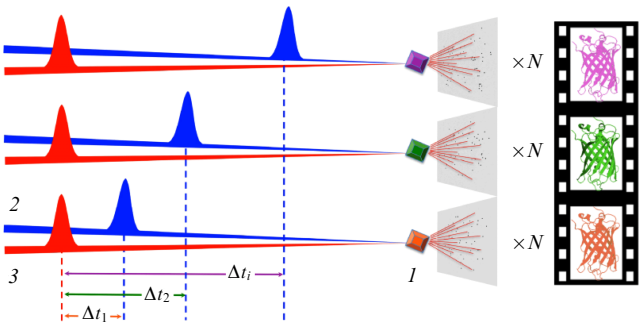

Figure 1. Principle of time-resolved crystallography. Sample *1* is investigated using X-ray (probe) pulses *2*. Time interval in diffraction experiment is determined by timing X-ray probe pulses *2* to pump pulses *3*. Evolution of structure of sample *1* in standard time Δt_i is controlled by changing delay Δt between pumping and probing. Each sequence of diffraction patterns is repeated N times to produce a complete data set from which a structural model can be determined [8].

delay is then changed to Δt_2 and the procedure is repeated. The structure determined at each Δt_i is a movie frame showing the conformational changes in the course of the reaction (Fig. 1) [8].

It is clear that in stroboscopic diffraction experiments the radiation pulses pumping the sample must be timed to the probing X-ray pulses. The duration of each X-ray pulse must be shorter than the lifetime of the induced excited state. But, at the same time, the duration of the measurement must not exceed the lifetime of the excited state, since then measurement will apply mostly to the structure of the ground state rather than the excited state. Since in the study of reversible processes the measurements are usually carried out on one sample, that sample must be sufficiently strong and radiation-resistant [4].

The temporal resolution Δt of traditional pump–probe experiments is determined by three factors: the duration of the pump pulse Δt_{L} that triggers the structural process, the probe X-ray pulse duration Δt_{Z}, and the temporal jitter of these two pulses Δt_{J} [9]:

$$\Delta\tau = (\Delta t_{\mathrm{L}}^2 + \Delta t_{\mathrm{Z}}^2 + \Delta t_{\mathrm{J}}^2)^{1/2}\,. \qquad (1)$$

Timing of pump pulse sequences (e.g., laser) and X-ray pulses must be achieved with jitter significantly smaller than the X-ray pulse width. However, achieving Δt_{J} values much lower than 1 ps is not trivial. Although ultrafast laser pulses with Δt_{L} values in the time range of tens of fs are easy to obtain, this is not the case for X-ray pulses. For example, the duration of the X-ray pulse Δt_{Z} emitted by synchrotron radiation (SR) sources is determined by the pulse duration of the electron bunch, which, in turn, is limited to 50–100 ps due to stringent requirements for the long-term stability of the electron beam [9].

3. Pumping methods

The critical moment of the experiment is the triggering of the dynamic process to be studied. The reaction should be initiated quickly and uniformly throughout the entire volume of the sample without its destruction. The complexity of this task lies in the fact that, due to the probabilistic nature of chemical and physical effects, it is, in principle, impossible to obtain 100% excitation of all molecules and atoms even in one crystal, and the thermal gradients and mechanical stress that arise with almost any technique of reaction initiation can lead to the destruction of the sample, up to its thermal explosion. Any physical or chemical parameter which the structure depends on is suitable for triggering the reaction [4, 10–12].

The pumping methods in use depend on the reaction to be triggered: UV or visible light activates light-sensitive proteins or so-called cellular compounds that form complexes with light-insensitive proteins [13]; a temperature jump shifts conformational equilibria [14–17]; X-ray irradiation can provide electrons that trigger redox processes [18] or the destruction of intermediate stressed states [19]; electric field pulses allow the study of protein mechanics [20]; and substrate diffusion initiates enzymatic catalysis [21, 22]. In diffusion mixing, the reaction is initiated by mixing the substrate with enzyme crystals [23]. The mixture is exposed to X-rays after a certain delay. By varying the time delay, the reaction can be followed on different time scales [24].

By far the most widely used method in the study of light-sensitive proteins is the optical trigger due to its simple technical implementation, the availability of a large number of samples with cyclic reactions that need to be studied, and the availability of ultrafast (fs–ps) time scales [25–27].

4. Radiation sources

To cover the broad time range of fundamental processes observed in nature, it is necessary to use different X-ray sources that differ in the duration of the probing pulses they produce: X-ray tubes with choppers, laboratory pulse units, SR sources, and X-ray free-electron lasers (FELs) [28].

4.1 Continuous radiation sources

Time-resolved X-ray diffraction experiments are conveniently performed using a sequential stroboscopic scheme [3]. Depending on the types of X-ray source, laser pump, and X-ray detector, there are two different schemes for carrying out measurements with the pump–probe method, as shown in Fig. 2.

In the first case (Fig. 2a), the probing X-ray beam consists of a sequence of short X-ray pulses $X(t)$, whose frequency determines the overall time scale of the experiment. During a single cycle, the dynamic process is initiated by exposing the sample to a short laser pulse, the effects of which are monitored after an adjustable time delay Δt. In the case of a molecular crystal, the sample's response to pumping can be of various types, e.g., a transient population of metastable state species, a change in the crystal symmetry detected by a time-dependent modification of the diffraction intensity, or the shape or position of the Bragg peak. The pumping laser pulses $S(t)$ are precisely timed to the X-ray pulse sequence by adjusting the desired time delay Δt. The signal scattered by the sample occurs only during the X-ray pulses $X(t)$, so a conventional integrating CCD or Image Plate detector is convenient. The pump–probe cycles are repeated until a satisfactory signal-to-noise ratio is achieved to provide a summed scattered signal at the detector, which is a signature of the transient structure of the sample averaged over $X(t)$. These experiments usually rely on the intrinsic time structure of pulsed sources.

In the second approach (Fig. 2b), a continuous X-ray beam is fed by a rotating anode tube or a conventional X-ray tube. During the pump–probe cycle, the structure of the

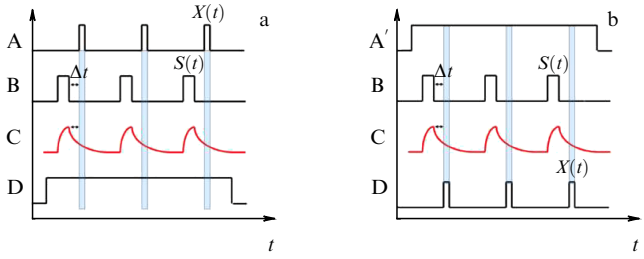

Figure 2. Measurement principle in pump–probe method using (a) pulsed X-ray radiation, (b) quasi-continuous X-ray beam and fast gated detector (A is pulsed source, A′ is continuous source, B is laser pumping, C is sample response, D is recorded signal, and Δt is time delay) [3] (see text).

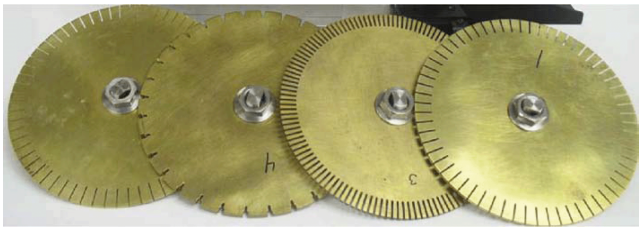

Figure 3. Mechanical choppers for application in time-resolved single crystal experiments [39].

crystalline sample and the signal recorded by the X-ray detector are constantly changing. In order to investigate the transient structure, the scattered signal is sampled by a fast-gating detector, such as a hybrid pixel detector [29–34], a streak camera, or an avalanche photodiode. Effective signal recording by the detector occurs only during a short adjustable window $X(t)$. In this case, the laser pulse serves as a trigger for detector gating and timing with an adjustable time delay Δt.

These two systems have different effects on the signal-to-noise ratio of the scattered X-rays (here, noise is considered to be the estimated standard deviation of the measured signal). In the first case, the X-ray detector receives the signal continuously, but scattering by the sample occurs only during the $X(t)$ pulses. If a CCD detector is used, the statistics of the experiments suffer from CCD readout noise and dark current. By contrast, the gated hybrid pixel detector is controlled by the photon counting statistics and does not suffer from dark current or readout noise. The signal detection is determined by adjustable time windows of measurement ($X(t)$ in Fig. 2b), whose width is limited only by the detector response time. Therefore, the hybrid pixel detector is highly advantageous for time-resolved laboratory experiments [3].

In the first case (Fig. 2a), for fast processes with lifetimes in the range from subnanosecond to ms, single SR pulses can be used. To study long-lived states with lifetimes in the range from 10 ms to 1 ms, such as triplet states of chemical interest, it is better to use a synchrotron X-ray beam in continuous mode (i.e., not to use its pulse characteristics) [35] or X-ray tubes with a rotating anode [36–38]. In this case, X-ray pulses can be generated using a rapidly rotating chopper wheel with narrow slits equally spaced on its circumference (Fig. 3). The task of such choppers is to very quickly close and open the X-ray beam, forming pulse trains with the desired duration Δt_Z and the interpulse time T.

If V is the chopper rotation speed in rpm and N is the number of slots, then the pulse repetition frequency in Hz

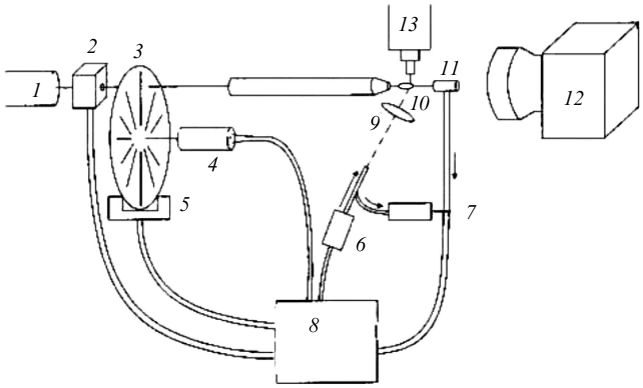

Figure 4. Schematic diagram of experimental setup for time-resolved diffractometry (*1* — continuous radiation source, *2* — shutter, *3* — chopper, *4* — motor, *5* — optical synchronization sensor, *6* — pulsed Nd:YAG laser, *7* — fluorescence detector, *8* — X-ray and laser pulse synchronization unit, *9* — lens, *10* — sample, *11* — photodiode plug, *12* — two-coordinate detector, *13* — optical microscope) [40].

(i.e., per second) will be determined by the expression

$$\upsilon_P = \frac{NV}{60}, \tag{2}$$

while the time between pulses (in seconds) is equal to

$$T = \frac{1}{\upsilon_P} = \frac{60}{NV}, \tag{3}$$

and the X-ray pulse duration becomes equal to

$$\Delta t_Z = \frac{w}{\pi D}\frac{V}{60}, \tag{4}$$

where w is the slot width and D is the chopper diameter.

By way of a practical example, for a chopper wheel with 240 300-μm-wide slots, 135 mm in diameter and a rotation speed of 4000 rpm, the X-ray pulse frequency (which should correspond to the laser pulse frequency) will be 16000 Hz and the opening time will be 10.6 ms [39].

Figure 4 depicts the experimental setup [40], in which a continuous radiation source and a chopper are used to generate a series of X-ray pulses.

The design of the chopper wheel with 32 radial slots 0.8 mm in width gives an X-ray beam chopping frequency of 6400 Hz at 12,000 rpm, which is slightly higher than the frequency of 5000 Hz at which the Nd:YAG laser provides maximum total power.

4.2 Synchrotron radiation

It is obvious that there is no way of using all the pulses of the primary X-ray SR beam; therefore, a special protocol is used on each channel of the source to extract a single X-ray pulse. The frequency of pump–probe cycles is determined by the electron bunch circulation time (for example, 2.82 μs at the European Synchrotron Radiation Facility (ESRF)) and the storage ring filling mode, conventionally subdivided into single-bunch (single-bunch mode) or multi-bunch mode.

Since the laser and X-ray pulses must be fed to the sample in pairs, a high-speed mechanical chopper is used to reduce the X-ray pulse repetition rate in the single-bunch mode of the storage ring (Fig. 5). In the multi-bunch mode, the procedure is more complicated. For example, the existing laser at the ID09 ESRF channel operates at 1 kHz; for comparison, the

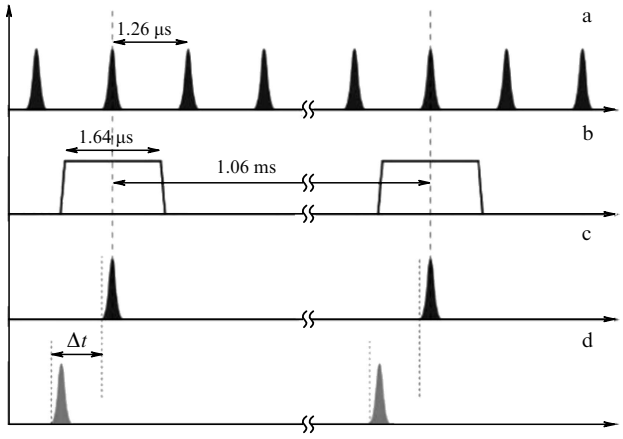

Figure 5. Time diagram of synchronization system using chopper to time 794-kHz X-ray pulses to 945-Hz laser pulses in a 1:1 ratio. Time settings are shown: SR pulses before chopper (a), chopper (b), X-ray (c), and laser pulses (d) on sample [46].

synchrotron produces 5.7-MHz pulses in the 16-bunch mode. The SR beam is first 'chopped' by a preliminary so-called thermal load chopper [41] into 36-μs pulses with a frequency of 1 kHz. These macropulses are then chopped by a high-speed chopper, a plane triangle with the rotation axis perpendicular to the beam propagation direction. It opens for 265 ns, which is sufficient to extract a single pulse. Details of the single pulse extraction technique are described in Refs [42–45].

X-ray pulses generated by third-generation synchrotrons have durations of the order of 50–150 ps and can be used to probe photoinduced structural changes on time scales > 100 ps using X-ray diffraction, scattering, or spectroscopy [47–49].

When use is made of a femtosecond laser pump pulse and an electronic tracking system to reduce jitter [50–54], the temporal resolution of the method is determined by the duration of the probing pulse. However, a temporal resolution of ~ 100 ps is insufficient to study fundamental chemical processes in biology, such as electron transfer (e.g., photosynthesis), isomerization (e.g., a retinal or p-cinnamic acid chromophore in photoactive yellow protein (PYP)), and the formation and breaking of covalent bonds (enzymes and heme proteins) [55].

Temporal resolution in the femtosecond regime at SR facilities can be obtained using the slicing method [56]. The slicing scheme was proposed by Zholents and Zolotarev [57], and its experimental verification was carried out by the authors of Ref. [58]. In the laser-electron slicing method, ultrashort (50–100 fs) laser pulses are collinearly overlapped and timed to the electron bunch of a synchrotron storage ring with a duration of ~ 30 ps inside an undulator tuned to radiation with the laser wavelength. The energy exchange between the light pulse and the electron bunch makes it possible to energetically modulate the short temporal slice of the electron bunch, which is then spatially separated from the main bunch using the dispersion of the electron-optical system [59–63].

Let us consider the possibilities of using SR in the pump–probe method.

4.2.1 X-ray microscopy. The search for new paths to high-density and ultrafast nonvolatile data storage devices has brought magnetic domain walls and vortices to the focus of attention of researchers. Vortices and domain walls can move at high speeds both when excited by a field and under the influence of current, whether sinusoidal or pulsed. It is the control of magnetic vortices through spin that scientists consider the basis for electronics of the future — spintronics. In spintronics, the movement of electrons from place to place or the flow of electric charges is not important for storing and processing information: the key role here is played by spin and the motion of electrons with a certain spin, the spin current. Information can be transmitted not by charge, but by spin, and not necessarily with the transfer of charged particles: they themselves may remain in place, but their spins will rotate, thereby transmitting information 'along the chain.'

The use of X-ray microscopy in the stroboscopic pump–probe mode (magnetic X-ray microscopy) opens up the possibility of high spatiotemporal resolution of spin patterns, which is necessary in the study of magnetodynamics.

Since pump–probe events can be repeated many times with fixed time delays in order to obtain a sufficiently high signal-to-noise ratio, the time resolution does not depend on the detector data acquisition rate. Therefore, both full-field transmission X-ray microscopes (TXMs) [64–68] and scanning transmission X-ray microscopes (STXMs) [69–72] are profitably used in the pump–probe mode.

Recall that a TXM consists of a condenser and an objective lens. The latter produces an enlarged image of the sample in the detection plane, which is recorded using a two-coordinate pixel detector. In an STXM, the objective lens focuses the X-ray (XR) beam onto a small spot on the sample, the sample is raster-scanned, and the intensity at the sample output for each scanning position is recorded by the detector. Most STXMs use detectors without spatial resolution, which integrate the radiation transmitted through the sample [73, 74].

Employed as a contrast mechanism for structure visualization in magnetic X-ray microscopy is the effect of X-ray magnetic circular dichroism, i.e., the dependence of the absorption coefficient of circularly polarized radiation on the direction of magnetization in a ferromagnet.

The stroboscopic TXM described in Ref. [75] is diagrammed in Fig. 6.

To ensure uniform illumination of the sample with a spot 20 μm in diameter, advantage is taken of a sectorial grating condenser (*4*) [76] consisting of 940 diffraction gratings measuring 25 by 25 μm. The sample is imaged with 700-fold magnification onto a two-dimensional pixel detector (*6*) using a Fresnel zone plate (*5*) with a diameter of 80 μm and a 50 nm-wide outer zone, providing a spatial resolution of the device as high as 65 nm. To excite the magnetic structure, short pulses of electric current (*2*) induce 186-ps-long magnetic field pulses in the sample (*3*). The excitation is timed to X-ray SR pulses (*1*), which probe the magnetization at different points in time Δt after pumping.

Presented in Ref. [72] are direct time-resolved images of the magnetization reversal of a micrometer-sized Permalloy ($Ni_{78}Fe_{22}$) element using a magnetic STXM (Fig. 7). The element is excited by a microwave signal superimposed on the field of a rectangular electric current pulse 2 ns in duration. The region of the natural resonant frequency of the magnetic element is identified by changing the microwave excitation frequency. The X-ray energy was tuned to the absorption edge of L_3Ni (852.7 eV), where the X-ray magnetic circular dichroism effect gives the highest magnetic contrast for Permalloy.

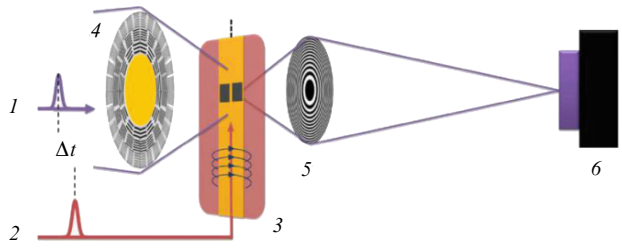

Figure 6. Schematic diagram of magnetic TXM: *1* — SR probe pulse, *2* — electric pump pulse, *3* — sample, *4* — sectorial grating condenser, *5* — objective lens, *6* — two-coordinate detector, Δt — delay time [75].

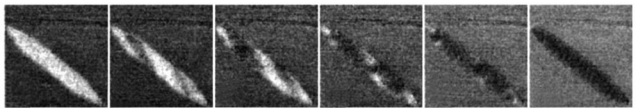

Figure 7. Images of magnetization reversal process in Permalloy element measuring 4 × 0.4 μm (pump pulse corresponds to $t = 1.27$ ns) [72].

In Ref. [77], an X-ray microscope in the pump–probe mode was used to observe thermal decomposition in a germanium single crystal due to laser-induced thermal diffusion. In the view of the authors of the work, its results will open up new possibilities for studying materials associated with laser-induced dynamic phenomena in solids on subnanosecond time scales, direct visualization of the evolution of laser-induced surface heating and melting, and the propagation of deformation waves in materials.

4.2.2 Laue diffraction. Time-resolved structural studies of specific proteins are aimed at revealing in detail the operation of a biological macromolecule and its interactions with other molecules in an organelle or organism [78]. Since many proteins are functionally active in the crystalline state, it is possible to perform 'kinetic' crystallographic experiments. In doing so, intentionally generated in the crystal are one or more intermediates, whose structures can be determined [10, 79, 80]. The approach relies on the use of Laue diffraction [81] and is mainly aimed at light-sensitive proteins that undergo repeated photocycles involving short-lived intermediates in the time range of 100 ps to 100 μs [82, 83].

In traditional synchrotron crystallography, diffraction patterns are obtained either by rotating the crystal during exposition to a monochromatic X-ray beam or by illuminating a stationary crystal with polychromatic X-rays. Both approaches ensure that all parts of the crystal, independent of any crystalline disorder, contribute fully to each spot of the entire diffraction pattern.

Processing monochromatic data does not call for analysis of the wavelength dependence of the scattering process or detector response and avoids the broadening of the reflection maxima inherent in the Laue method. However, using monochromatic radiation implies a very inefficient use of photons in the synchrotron beam and, therefore, longer periods of X-ray probing, thereby limiting the achievable time resolution.

By abandoning the monochromator and using only a mirror to reject high-energy X-rays, it is possible to obtain a 'pink beam' with a relative photon energy spread $\Delta E/E \approx 5\%$, with a flux approximately 100 times higher than that of a monochromatic beam. Similarly, improving the throughput reduces the number of images, which in turn reduces the experimental time.

Another advantage is that most of the reflections are complete when use is made of pink X-ray sources: slightly different wavelengths will fully image the block crystal. For the same reason, one would expect to get more reflections in the diffraction image.

However, since the resultant reflections are generated in a specific wavelength range, reduction to a single set of structure factors requires knowledge of the spectral distribution of the incident beam and other wavelength-dependent effects such as absorption, anomalous scattering, and detector energy dependence. In practice, all wavelength-dependent effects manifest themselves in the 'λ curve,' which, in most programs, including PRECOGNITION [78, 84], is derived from the intensities of equivalent reflections collected several times at different wavelengths and requires relative scaling of the frames in the data set.

An elegant modification of diffraction experiments is the RATIO method, which uses a probe–pump–probe sequence and the ratio between the X-ray intensities prior to and after pumping [85, 86] or between an independent reference intensity and the intensity after pumping [87].

The RATIO method provides wavelength-independent results, does not assume isotropic radiation absorption, and does not require relative scaling of different frames, since paired frames are collected at the same temperature and under the same sample conditions. This eliminates a number of uncertainties inherent in standard processing of Laue diffraction data. To fully utilize the method, the intensity of each reflection when the laser is turned on and off must be collected immediately after each other, eliminating variations in the X-ray beam intensity over long distances, the effects of slow radiation-induced sample degradation, and differences in absorption corrections.

Data analysis is one of the most complicated aspects of the polychromatic Laue diffraction method. The first step in processing Laue diffraction patterns is indexing. Automatic indexing algorithms implemented in widely used software, including MOSFLM [88], XDS [89], and DirAx [90], were initially developed for data collected in the sample rotation mode with the use monochromatic radiation. Usually, they perform poorly when the sample is exposed to a pink beam due to their dependence on specific experimental conditions. Modern programs that provide indexing of single broadband diffraction patterns of macromolecular crystals are PRECOGNITION [78, 84] and PinkIndexer [91].

The information needed to determine the protein structure is encoded in the relative intensities of the observed diffraction patterns. Once the indexing problem has been solved and the partial intensities have been scaled and combined, the integrated intensities can be converted to amplitudes using standard techniques [92]. Once the amplitudes of the structure factors have been found for all time delays, difference Fourier maps and then time-dependent difference electron density distributions can be calculated. These distributions can then yield structural and mechanistic quantitative information [7, 9].

Recent years have seen the development of quite advanced software for processing Laue diffraction data, which provides accuracy, automation, and speed [85, 93]. For example, problem-oriented software such as LAUEUTIL, [94, 95] and PRECOGNITION [78, 84] have been developed. These programs offer different approaches to solving these issues

[93]. These two tools, although they aim to solve the same problems, are in fact fundamentally different in terms of the approach they implement. While PRECOGNITION is more general purpose and its algorithms are designed to favor macromolecular systems, LAUEUTIL is designed to process Laue data collected from small and medium-sized crystalline molecules.

There are a series of studies concerned with both macromolecular [42, 44, 78, 84, 96, 97] and low-molecular systems [98–102] using the pump–probe method.

Temporal resolutions ranging from $\sim$ 100 ps to 5 ns were achieved in studies of myoglobin [103–107], dimeric hemoglobin [83], photoactive yellow protein (PYP) [13, 82, 108], the organic molecule 1,4-dibromo2,5-bis(octyloxy)benzene [38], and the CuI complex [109].

The above examples testify to the fact that the pump–probe method can be successfully employed in protein crystallography.

Laue diffraction has also found application in the study of self-propagating high-temperature synthesis (SHS), which is among the promising techniques for producing refractory compounds. The reaction is initiated by a powder charge and develops further due to the heat released during the reaction. The initial sample is a pressed tablet of a mixture of powders of the initial components. When the reaction is initiated from one side of the sample, the reaction front moves along the sample at a speed of several millimeters to several ten meters per second. The temperature in the reaction zone can reach 5000 °C, which allows the synthesis of refractory compounds [110].

Modern SR beam technology makes it possible to investigate structural changes of matter during SHS with a time resolution of about 5 ms and to obtain fundamentally new, previously inaccessible information about the kinetics of a chemical reaction and the occurrence or absence of intermediate phases [111–113].

The first experimental data on SHS were obtained about 40 years ago in Novosibirsk [114, 115]. Different intermetallic compounds were subsequently studied. For example, Ni and Al, as well as materials based on them, are of interest for the production of high-temperature materials, protective coatings, catalysts, etc. The Ni–Al system is an interesting and complex subject for such studies due to the large number of phases, both ordered and disordered, that can be formed during the synthesis of the final product. Therefore, knowledge of the sequence of phase transformations is important for practice, as well as for researchers studying the mechanisms of solid-phase reactions.

The results obtained in Ref. [112] indicate that the NiAl compound is formed in the first milliseconds after the onset of the reaction in the combustion wave. The ordering of this phase can continue behind the combustion wave front. The changes in the diffraction patterns observed after passage of the combustion front are attributable to recrystallization, grain size growth, and ordering in the nickel monoaluminide.

The data obtained by the authors of Ref. [111] provide grounds for dividing the reaction into stages. In the first stage (0–20 ms), the intensity of the Ni peak decreased, while the intensity of the Al peak remained approximately the same; peaks of intermetallic compounds and other phases were not observed. In this case, the liquid phase was not formed (the intensity of diffuse scattering was low). The second stage took place during the next 20–45 ms. It was accompanied by a further lowering of the Ni peak, a lowering of the Al peak, and the emergence of a new intermetallic peak. Simultaneously, melting occurred (an increase in the intensity of diffuse scattering was observed). The Al peak disappeared at the end of this stage (presumably, the Al melted and liquid Al reacted with Ni particles to yield NiAl. The next stage lasted for 70–80 ms from the start of the reaction. Ni particles continued to react with molten Al until they were completely consumed by the reaction. During the last stage (80 ms–70 s), the Debye ring of the intermetallic compound split into separate spots. The spot intensities would increase, suggesting a recrystallization process.

4.2.3 Small-angle and wide-angle scattering. Although Laue diffraction is an excellent tool for studying the structural dynamics of macromolecules, it has two major drawbacks. First, the method is applicable only to proteins that can be crystallized. Second, the structural dynamics studied by Laue diffraction occur in the crystalline phase and may differ from the dynamics that occur in an aqueous environment, which is the physiological state of living organisms. For example, large conformational changes such as protein folding/unfolding can disrupt the crystal lattice. Since most biological functions of living organisms are executed in solution, it is desirable to observe structural changes in proteins in solution. In this connection, scattering by solutions is relevant for observing the motion of proteins in their physiological states [116]. Therefore, time-resolved solution X-ray diffraction (scattering by solutions) was developed [117, 118], a method called liquidography.

The advantage of in-solution scattering over time-resolved X-ray protein crystallography is that it can probe irreversible reactions and large-scale conformational changes that cannot take place within the crystal [45, 119].

However, visualizing reaction dynamics in solution is not as straightforward as for reactions in the crystalline phase, since the molecules in solution are unevenly distributed and randomly oriented. As a result, solution samples produce centrosymmetric scattering patterns rather than Bragg spots (Fig. 8), so solution scattering inherently provides a lower spatial resolution than protein crystallography does.

To calculate the X-ray scattering intensity, advantage can be taken of programs like CRYSOL and FoXS [120, 121]. The parameter $\Delta S(q, t)$, which is the difference between the X-ray scattering intensities at the time delay (t) and the reference time delay (t_{ref}), can be expressed as follows [122]:

$$\Delta S(q, t) = S(q, t) - S(q, t_{\mathrm{ref}}). \quad (5)$$

One-dimensional difference curves $\Delta S(q)$ are multiplied by q to increase the intensity at large scattering angles ($q = (4\pi/\lambda)\sin(2\theta/2)$, where λ is the X-ray wavelength and 2θ is the scattering angle). The $q\Delta S(q)$ curves contain direct

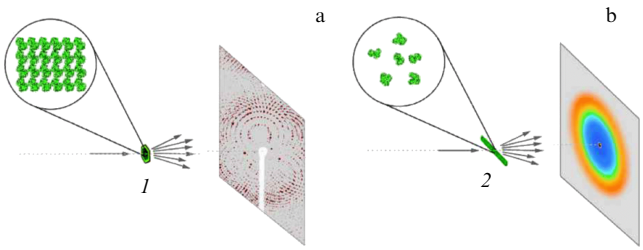

Figure 8. Time-resolved X-ray diffraction by protein crystals (*1* in Fig. a) and X-ray scattering by protein solutions (*2* in Fig. b) [45].

information in the q-space about structural changes in the solute and solvent.

In the solution phase, however, the solute molecule of interest is surrounded by a large number of solvent molecules that do not directly participate in the reaction, and the solution scattering pattern is dominated by the contribution of the solvent molecules. To minimize the contribution of the solvent, difference scattering curves are obtained by taking into account the difference between the scattering curves measured before and after the reaction initiation. After a series of time-resolved difference scattering curves are measured at different time delays, they can be kinetically analyzed using a method based on singular value decomposition (SVD) [97, 123] or principal component analysis (PCA) [124]. Kinetic analysis allows exposing the dynamics of protein conformational changes [116, 122].

For low q values, all protein electrons scatter in phase, which significantly increases the protein contribution to the scattering intensity against the solvent background. The protein scattering pattern is more or less featureless for $q < 0.1\,\text{Å}^{-1}$. At higher q values, the structured pattern appears primarily due to correlations among protein subunits ($0.15 < q < 0.25\,\text{Å}^{-1}$), helices, or sheets ($0.25 < q < 0.6\,\text{Å}^{-1}$), and among atoms forming secondary structures ($q > 0.6\,\text{Å}^{-1}$) [125–127].

X-ray radiography of solutions can be conventionally divided into two domains: of small-angle X-ray scattering (SAXS) with a range of q from 0 to $0.3\,\text{Å}^{-1}$ and wide-angle X-ray scattering (WAXS) ($0.2 < q < 1.0\,\text{Å}^{-1}$) [128].

The SAXS domain is sensitive to protein size and shape [129], while the WAXS domain provides additional structural information at higher resolution [130].

Studied using SAXS were structural changes of proteins in solution due to different perturbations, including a temperature jump caused by a laser [15, 131, 132], a pH jump [133], photoreduction [119], photorelease of ATP (adenosine triphosphate) [134, 135], and direct photoexcitation [136–138].

The WAXS method, which was based on earlier studies of the reaction dynamics of small photochemical molecules [139–141], was used to study ultrafast protein dynamics [142] triggered by light, such as photodissociation of CO from the heme groups of myoglobin [143–145], homodimeric hemoglobin [127], as well as reactions caused by isomerization of the chromophore in the photoactive yellow protein [146, 147], bacteriorhodopsin [148], and proteorhodopsin [148, 149].

It is noteworthy that the first experiments using SAXS in the pump–X-ray probe mode commenced in 1973 at the Siberian SR Center by the A.A. Vazina group [150]. The subjects of the study were isolated fibers and intact muscles of frogs, fish, and insects.

Furthermore, experiments were performed at the Siberian SR Center to study the type and mechanism of destruction of the condensed phase, as well as the growth dynamics of new formations, including crystalline ones [110, 151–154].

In the detonation of explosives with a high carbon content, a significant fraction of condensed residue is observed along with gaseous explosion products. The condensed residue consists of carbon in different phase forms. Constant attention to this problem is due to the need to take this feature into account, on the one hand, for describing detonation and explosive flows and, on the other hand, for the technologically simple detonation synthesis of carbon nanoparticles, including diamond ones. The use of SAXS makes it possible to determine the dynamics of a number of averaged characteristics of the condensed phase. Proceeding from the integral SAXS intensity, with the inclusion of the changing contrast of the medium, the formation time of the total fraction of condensed carbon is estimated without distinguishing between the shapes and sizes of the particles produced. For charges based on triaminotrinitrobenzene (TATB) 20 mm in diameter, it amounts to about 2 μs. The dynamics of the average particle size for charges of different explosives was determined from the angular SAXS distribution [152].

The first results concerning the production of nanosized diamonds obtained in an explosion were presented in 1989 [155]. It was assumed that the synthesis was determined mainly by the chemical reaction zone proceeding from the constancy of the particle size distribution of nanodiamonds in the purified products (retained after the explosion) for different sizes of explosives [155]. However, in Refs [156, 157], it was shown that condensation occurred outside the chemical reaction zone.

4.2.4 Absorption spectroscopy. X-ray absorption spectroscopy using SR is a well-established method that allows obtaining information about the electronic, structural, and magnetic properties of substances.

Depending on the energy range, X-ray absorption edge spectroscopy is divided into two parts:

(1) the low-energy domain, where multiple scattering of a photoelectron is significant, called the near or near-threshold fine structure: XANES (X-ray Absorption Near Edge Structure);

(2) the high-energy region, called the extended or far fine structure: EXAFS (Extended X-ray Absorption Fine Structure), where the main contribution to absorption is made by single scattering of a photoelectron.

X-ray absorption spectra are characterized by absorption edges (K, L, M...), which are unique to the type of absorbing atoms, and by fine structures in the low-energy domain near the absorption edge (XANES) and in the high-energy domain, from tens to hundreds of eV above the absorption edge (EXAFS).

In the XANES mode, a significantly larger number of surrounding atoms are involved in the scattering process than in the EXAFS mode, atoms not only from the first coordination sphere participating in the scattering, but also from spheres located at significant distances from the absorbing atom. Analysis of XANES spectra allows obtaining information on the local arrangement of atoms around the absorbing atom, including valence angles, which hardly affect the EXAFS spectrum [158].

Clearly, in combination with optical lasers, time-resolved X-ray absorption spectroscopy is a powerful tool for tracking the dynamics of electronic systems [159, 160] and their structures [161]. The experimental simplicity makes this method attractive for different research areas, including materials science, biology, and chemistry [162].

The valence state information provided by XANES is used to follow the dynamics of a wide range of charge transfer processes (e.g., catalysis and metal-ligand charge transfer), while EXAFS can provide detailed information on the structural shifts occurring in the molecule due to bond length changes in metastable states [93]. Furthermore, EXAFS is capable of simultaneously monitoring the geometric structure

with a high spatial resolution. These properties make the new tool suitable for studying different phenomena in rather complex systems, even in disordered environments. Therefore, it seems possible to study, for instance, the very first moments of biological activity of proteins in physiological environments [163].

The majority of studies on pump–probe X-ray absorption spectroscopy have been carried out on the picosecond time scale (e.g. [161, 163–171]). Experiments using a streak camera as a detector with a resolution of a few ps have been reported [172], as has the use of an SR beam slicing scheme to achieve subpicosecond time resolution [159, 173–175].

A wide range of objects and phenomena have been investigated, such as photoinduced changes in the electron charge distribution, molecular structure, and spin state of Fe(II) polypyridyl complexes [173, 176], electron localization in photoexcited TiO_2 anatase [175], the nature and lifetime of electron traps at room temperature in TiO_2 [177], electronic changes resulting from a photoinduced ultrafast insulator-to-metal phase transition in VO_2 crystals [174], the dynamics of substitution of $Fe(CO)_5$ ligands in ethanol [164], light-induced electron transfer and associated structural and spin changes occurring in two photoexcited heterobimetallic ruthenium–cobalt complexes [178], characterization of electronically excited states of Cu(I) complexes [179], anisotropic elastic deformation of the unit cell of $BiFeO_3$ film [180], hole trapping in an aqueous medium by ZnO nanoparticles [181], modification of the electronic state and the decomposition process of WO_3 after photoabsorption [182], light-induced electron transfer and associated structural and spin changes occurring in two photoexcited heterobimetallic ruthenium–cobalt complexes [178], and the observation of the electronic states of photoexcited hematite [183]. It has also been shown that time-resolved absorption spectroscopy can be profitably employed in the *operando mode* [184, 185].

4.2.5 Photoelectron spectroscopy. X-ray photoelectron spectroscopy (XPS) is one of the most powerful methods for the nondestructive quantitative analysis of the chemical composition and electronic structure of surfaces and interfaces. This method enjoys wide use in many areas of research and industry due to its capability of obtaining quantitative information on the atomic composition and electronic structure of solid and liquid surfaces. In particular, in the area of surface physics and interfacial chemistry, it has evolved into a powerful spectroscopic tool that not only reveals the presence of small traces of atomic species on a surface based on their characteristic electron binding energies, but also provides insight into their chemical environment. For example, the simultaneous sensitivity of time-resolved XPS to the dynamics of charge carriers within a semiconductor substrate and the electronic configuration of adsorbed molecules makes it possible to study the dynamics of electron charge flow across hybrid molecule–semiconductor interfaces [186].

Figure 9 shows a schematic of the experimental setup for XPS with the use of the soft X-ray part of the SR spectrum of an advanced light source (ALS) to monitor the dynamics of photoinduced electrons at the interface formed by N3 (Ruthenium 535) molecules deposited on a ZnO substrate. The setup provides 150-ps-long X-ray pulses with an energy of 635 eV. Visible light pulses ($\lambda = 527$ nm) from a diode-pumped laser (*2*) are injected into the vacuum chamber through a vacuum viewing window in the rear part of the

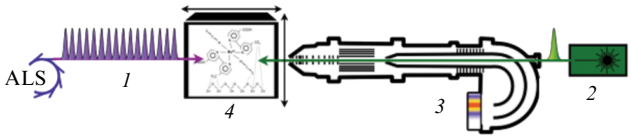

Figure 9. Schematic diagram of XPS setup on ALS: *1* — SR pulse packet, *2* — laser, *3* — analyzer, *4* — sample [174] (see text).

hemispherical analyzer (*3*) and along the central axis of the electrostatic lens system onto the sample (*4*). The coaxial arrangement of the laser beam and the lens system of the electron hemispherical analyzer significantly simplifies the alignment procedure of the experimental installation [187].

Time-resolved photoemission spectroscopy measurements to track the change in surface potential after the action of surface photoEMF on an atomically clean Si(111) 7×7 surface [188], studies of the relaxation of the surface photoEMF effect on atomically controlled In/Si(111) surfaces [189], and a study of electron-hole recombination on the (0001) surface of a ZnO single crystal [190] were performed at the BL07LSO line of the SPring-8 synchrotron center [191].

4.2.6 Diffraction by single crystals. X-ray diffraction is likely to be the best-known method for studying the structure of single crystals at the atomic level. Parameters of the diffraction reflection curve (rocking curve), such as its position, integrated intensity, and width at half maximum, provide information on structural imperfections of the single crystal, such as deformation and mosaicity degree.

Using Bragg's law, the authors of Ref. [192] transformed the measured shift of the diffraction reflection peak of the Ge(111) crystal into the spatial profile of the deformation generated by photoabsorption of the pump pulse.

In Ref. [193], the modulation of the charge density wave (CDW) and the lattice deformation of single crystal chromium (Fig. 10) were studied using picosecond X-ray diffraction as a function of the time elapsed after femtosecond laser excitation. The authors of the study provide evidence for the existence of transient shear CDW deformation, which disrupts the symmetry of the lattice sites. This deformation is characteristic of sliding CDWs, as is observed in other incommensurate CDW systems, suggesting the possibility of laser-induced sliding of CDWs in three-dimensional systems. In the authors' opinion, this result opens up prospects for unconventional laser transport of correlated charges.

However, the small number of diffraction studies of single crystals with the use of picosecond X-ray SR pulses indicates that shorter (subpicosecond or even femtosecond) probe pulses should be used to study fast processes in single crystals. Here, laboratory pulsed X-ray sources are an aid to the researcher.

4.3 Pulsed laboratory sources

Laboratory sources, also called table-top sources, vary in pulse duration, energy range, energy tuning capabilities, etc. Commonly used table-top sources include: (1) betatron radiation sources, which can produce pulse durations down to several fs [194]; (2) high harmonic generation (HHG) sources, which can provide attosecond pulse durations but are limited in energy range from vacuum ultraviolet to soft X-rays [195]; and (3) laser-driven table-top plasma sources, which can generate hard X-rays with pulse durations of 100 fs [47].

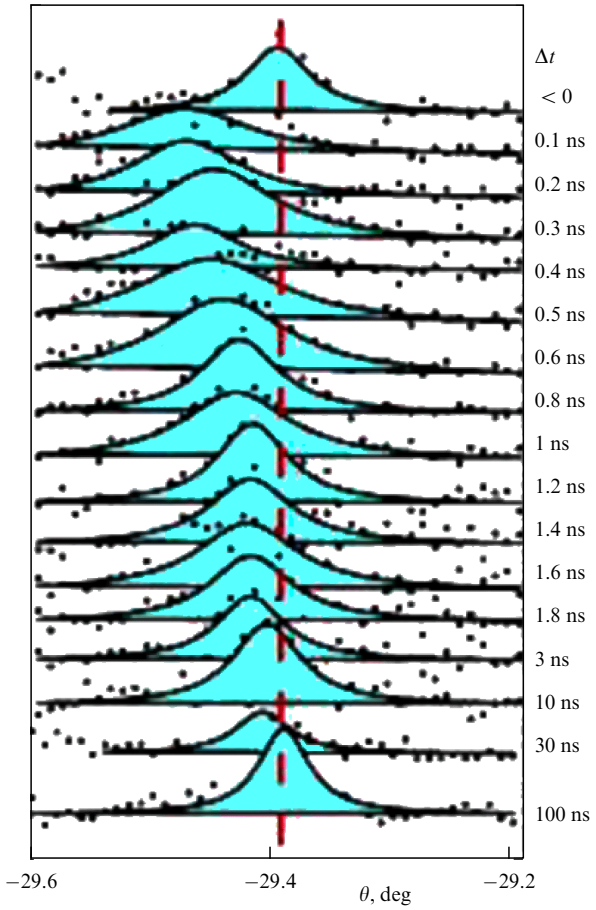

Figure 10. Change in position, area, and shape of rocking curve of Cr(011) single crystal depending on time delay Δt. Position of maximum measured in absence of pump pulse is shown by dashed line (θ — Bragg angle) [193].

4.3.1 Betatron radiation. In the interaction of laser radiation with gas targets, the leading edge of a high-power laser pulse ionizes the gas, and its main part excites a wake wave in the gas. This wave propagates in the plasma with a velocity close to the group velocity of the laser pulse and has a large longitudinal electric field, which is employed for particle acceleration. At the same time, the transverse fields of the wake wave entail oscillations of the accelerated electrons, called betatron oscillations, which are responsible for the generation of betatron radiation, the energy of which for highly relativistic electrons is in the X-ray range, which extends to approximately 10 keV. The characteristics of betatron radiation, such as collimation (~ 10 mrad), short pulse duration, and good spatial coherence, turn out to be suitable for studying the structure of a wide class of objects [196, 197]. Another advantage of betatron radiation is its timing to the original laser pulse. This allows the X-ray radiation to be precisely timed to the optical pulse [197].

Time-resolved measurements of the ionization state of warm dense aluminum [197] and copper foil [198] were carried out using betatron radiation and absorption spectroscopy.

4.3.2 High-harmonic generation. Pulses with far shorter wavelengths down to a few nanometers (corresponding to photon energies of hundreds of eV) can be obtained by high-harmonic generation from noble gas atoms. In HHG, an intense laser pulse is focused into the gas, where strong-field ionization converts a (small) fraction of the incident light into much shorter wavelengths. The strong electric field of the laser ionizes an electron, pulls it away from the parent ion, and then throws it back, generating coherent radiation [199]. Attosecond light pulses (with the current record set at 53 as [200]) are beginning to be used in time-resolved spectroscopy to provide direct access to the electron dynamics in molecules, and ultrashort pulses with even higher photon energies, up to hard X-rays, provide access to time-dependent structural dynamics [59]. This explains the awarding of the 2023 Nobel Prize in Physics to Ferenc Krausz, Anne L'Huillier, and Pierre Agostini for methods of producing ultrashort attosecond radiation pulses and for the opportunity thereby opened up to study ultrafast electronic processes inside atoms and molecules.

In Ref. [201], HHG produced broadband X-ray pulses (from ~ 160 to 310 eV with a duration of less than 50 fs), which were used to study the photoinduced ring opening reaction of 1,3-cyclohexadiene using femtosecond X-ray spectroscopy near the carbon K-edge (~ 284 eV).

Reported in Ref. [202] was the implementation of time-resolved femtosecond absorption spectroscopy using HHG covering the spectral region from 280 to 530 eV to monitor light-induced chemical reactions in the lowest electronic states of isolated CF_4^+ and SF_6^+ molecules in the gas phase.

Presented in Ref. [203] was an instrument for attosecond X-ray spectroscopy covering the absorption edges of most light elements from the L-edge of silicon to the K-edge of nitrogen. This instrument combines an attosecond table-top HHG source and infrared pulses excited by 11-fs-long pulses with an power of 1.7–1.9 mJ and duration shorter than 11 fs with a wavelength of 1.76 μm. Surprisingly low temporal jitter (20 as) was achieved due to active stabilization of the pump and probe channels. A temporal resolution of better than 400 as was obtained in measurements at the $L_{2,3}$-absorption edges of argon. In combination with a high photon flux, this instrument, according to the authors of the work, opens the way to attosecond spectroscopy of organic molecules in the gas phase or aqueous solutions, as well as thin films of modern materials.

4.3.3 Plasma sources. In laser-driven plasma sources, probe pulses are generated by focusing very intense femtosecond optical laser pulses onto a metal target to produce hard X-ray pulses of characteristic Kα radiation with a typical duration of ~ 100 fs [3, 204–209]. An interesting consequence of using a plasma source in the pump–probe mode is the absence of timing jitter, since the same optical laser is used to excite the sample and generate the plasma [6, 210] (Fig. 11).

Table-top ultrafast plasma X-ray sources enjoy wide use in time-resolved X-ray diffraction and spectral studies of photoinduced structural dynamics in single crystals. Ultrafast lattice deformation of metallic crystals tens to hundreds of nanometers in thickness after femtosecond laser excitation can be measured directly using subpicosecond X-rays and a femtosecond electron pulse. For example, 100-fs optical pulses were used in Ref. [211] to heat 150-nm-thick Au(111) crystals below the melting point, and 0.6-ps-long X-ray pulses were used to monitor the subsequent structural evolution with subpicosecond time resolution. By monitoring the energy- and time-dependent modulation of the rocking curve width and offset, information was obtained on electron-phonon interaction, photon-lattice interaction, and the time-resolved kinetics of crystalline disorder.

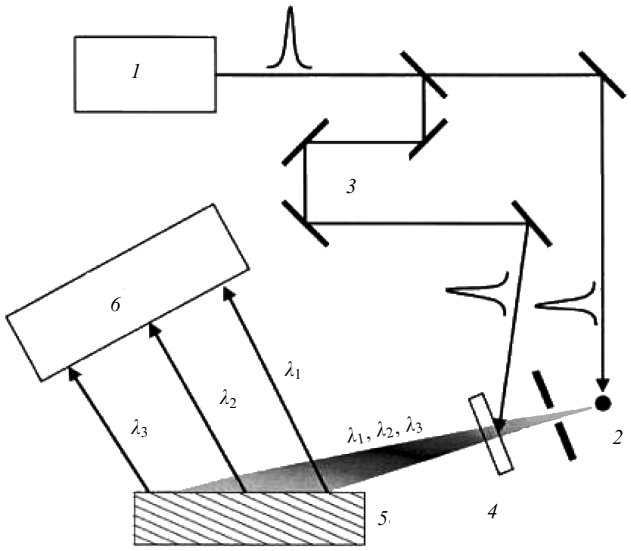

Figure 11. Schematic diagram of dispersive X-ray spectrometer for time-resolved studies (*1* — laser, *2* — metal target serving as X-ray source, *3* — time delay unit, *4* — sample, *5* — crystal analyzer, *6* — detector) [210].

In Ref. [212], compression of the crystal lattice was observed during the first few ps after laser irradiation of an aluminum single crystal, which was attributed to the generation of an explosive force and the propagation of elastic waves. In Ref. [213], it was determined how ultrafast heating occurs in the depth of the skin layer and how heat exchange occurs from the surface (skin) layer to the volume of a ferromagnetic Ni(111) crystal with a thickness of 150 nm.

Reported in Ref. [214] was an analysis of the polarization and lattice dynamics in a metal/ferroelectric/metal nanolayer system by femtosecond X-ray diffraction. Optical excitation of $SrRuO_3$ metallic layers produces giant stresses (> 1 GPa), which compress $PbZr_{0.2}Ti_{0.8}O_3$ layers to 2% and entail a strong suppression of the ferroelectric polarization. It was also shown in [215] that spatially periodic femtosecond excitation of the GaAs/AlGaAs superlattice leads to coherent lattice motions with a period of 3.5 ps, which were directly monitored using femtosecond X-ray pulses with a repetition rate of 1 kHz.

Also reported was the use of X-ray absorption spectroscopy to study the structural evolution of 100-nm-thick aluminum foil with a time resolution of 3 ps under ultrafast laser heating and ablation [216, 217]. The X-ray absorption spectra testify to an ultrafast transition from a crystalline solid to a disordered liquid with a subsequent gradual transition from a delocalized valence electron structure (metal) to localized atomic orbitals (nonmetal–vapor) as the average interatomic distance increases.

However, the insufficiently high X-ray photon flux compared to ultrashort X-ray sources such as X-ray FELs in many aspects limits the use of laboratory pulsed sources.

4.4 Free-electron lasers

FELs generate extremely bright (9–10 orders of magnitude brighter than third-generation synchrotrons) and extremely short-duration (fs) pulses of coherent X-ray radiation. With such unprecedented properties, they allow experiments to be carried out in the pump–probe mode with femtosecond time resolution.

FELs are a truly revolutionary technology. Single ultrashort femtosecond X-ray pulses are so intense that the atoms of the object under study are completely ionized, and all experiments become destructive. What saves the situation is that the destruction does not occur instantly. There is a short time interval in the range of 100 fs between the irradiation of a tiny biomolecular crystal, usually 1–10 microns in size, by an X-ray pulse and the complete loss of its structure and the recording of a diffraction pattern. The diffraction pattern can be obtained in this time window [218]. One tiny crystal yields one diffraction pattern. A complete data set with sufficient resolution can be collected by sequentially introducing a large number of small, randomly oriented crystals into the FEL beam. Due to good spatial coherence, the FEL beam can be focused onto a nanometer-sized focal spot. In this case, crystals with an edge length of the order of several nanometers can be injected into the beam and analyzable diffraction patterns can be obtained [45, 219–221]. To ensure uniform irradiation, the crystal size must be equal to or smaller than its extinction length, which is about 5 μm [27] for the photoactive yellow protein [222]. This technology is called 'serial femtosecond X-ray crystallography' [223].

So, a time-resolved crystallographic experiment can benefit from ultrashort FEL pulses [5] provided that the reaction itself can be initiated on a similar time scale. In these cases, it is potentially possible to achieve the ultimate time resolution provided by an X-ray pulse [21].

The use of FEL pulses in combination with readily available femtosecond optical pulses has opened up the possibility of investigating dynamics with durations of several fs. The technique is called 'sequential time-resolved X-ray crystallography' and allows tracking reversible or irreversible conformational changes, since microcrystals are destroyed after only one X-ray image [21]. Thus, light-stimulated reactions can be investigated on previously unprecedented femtosecond time scales.

FELs have fostered the rapid development of new X-ray detectors to keep pace with increasing data rates and improve experimental precision. New generations of integrating detectors, which measure the total charge after a set exposure time, have similarly high sensitivity and frame rates. They include the CSPAD [224] and the ePix [225, 226] and JUNGFRAU [227] integrating detectors. A new detector, called the Adaptive Integrating Pixel Gain Detector (AGIPD) [228], has been developed to cope with higher pulse rates. The maximum achievable readout rate of the AGIPD is 3520 Hz [228], increasing the data acquisition rate by almost 30 times compared to the CSPAD.

In order to exploit the full potential of FELs and extend their applicability to the study of condensed matter (especially biological samples), sample delivery is one of the key research areas when using serial crystallography [229].

4.4.1 Methods of Sample Delivery. Since the sample is eventually destroyed by the intense X-ray pulses, a reliable method of replenishing the microcrystals at the intersection of the pumping and probing pulses is needed. This can be accomplished in two main ways: the sample can be delivered to the irradiation domain using a special injection device, or the samples can be fixed to a rigid support (fixed target), which is then raster scanned, allowing a new sample to be irradiated each time (Fig. 12).

The Gas Dynamic Virtual Nozzle (GDVN) injector [231] was one of the first and still remains one of the most widely

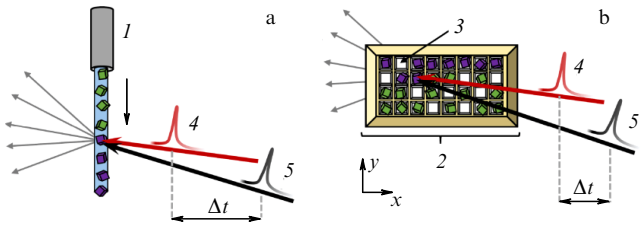

Figure 12. Methods of sample delivery for serial crystallography. In microfluidic version of experiment (a), crystals are delivered into X-ray beam using microfluidic nozzle *1* with a diameter of tens to hundreds of micrometers. Flow of randomly oriented microcrystals continuously flows perpendicular to pulsed X-ray beam. In version with a fixed target (b), microcrystals of random orientations are mounted on solid support chip *2* containing windows *3* of appropriate size; chip is rapidly moved through pulsed X-ray beam in x and y directions. Each crystal yields one diffraction pattern corresponding to a random slice of reciprocal space (*4*, *5* are light and X-ray pulses, respectively, Δt is delay time) [230].

used injectors for serial time-resolved X-ray crystallography. Crystals in the mother liquor are delivered into the X-ray beam employing a microfluidic nozzle with a diameter of tens to hundreds of micrometers. The main disadvantage of the GDVN injector is a high sample flow rate. With a typical flow rate of 10–40 μL min^{-1} [232], a complete data set requires up to several hundred milligrams of crystallized protein, which is unfeasible for many targets, membrane proteins in particular.

To obviate this problem and reduce sample consumption, a special device for introducing a viscous medium, also known as a Lipidic Cubic Phase (LCP) injector, was developed [233]. The LCP is a liquid crystalline gel-like mesophase that mimics the native membrane environment, supporting the crystallization of membrane proteins. The LCP crystallization method has proven to be very successful for a variety of membrane proteins. Crystals of soluble proteins can also be grown in the LCP or mixed with it after growth for higher-efficiency sample delivery [234].

Another type of reaction trigger has been developed, involving mixing with a ligand or substrate for serial X-ray crystallography: Mix-and-Inject Serial Crystallography (MISC) [21, 235, 236]. MISC is a method designed to study enzyme-catalyzed reactions in which protein microcrystals are mixed with a substrate and then probed by an X-ray pulse. So, MISC as a convenient way to initiate a reaction opens up a new area of investigation of biological reactions triggered by a substrate or ligand. The rate of substrate diffusion into microcrystals limits the temporal resolution of MISC [237].

A proven mixing injector developed by Wang et al. was a version of the GDVN in which the central sampling line was replaced by coaxial feed lines for the crystal solution and the reagent solution [238]. In this device, the two solutions were pre-mixed by diffusion and focusing into a free stream of liquid.

In practice, high-concentration samples tend to aggregate and may clog the capillaries and nozzles employed for their delivery. Therefore, most experiments are usually performed at concentrations below the optimal one, which further lowers the efficiency of the method. The root of this inefficiency lies in the delivery of the sample under the action of the pump pulse in a continuous flow. Therefore, it is reasonable to look for a pulsed injection technique that can deliver crystals synchronously with the arrival of the pump pulse (Drop-on-Demand). Several attempts have been made in the past to achieve this using piezoelectric [239] or acoustic [240] droplet injection, segmented flow [241], and on-tape [242] injection. The inability to maintain stable and continuous timing to the pump pulses and the formation of large droplets or unstable jets are just a few of the unsolved problems limiting such injection methods. A new 'catch and release' approach proposed by the authors of Ref. [243] produces locally concentrated crystal clumps, thereby significantly reducing the required initial crystal concentration and the amount that has to be prepared.

An alternative is to perform single experiments with a sample mounted on a thin solid membrane (chip) [244–246]. In this case, instead of continuously incoming samples, each pump pulse and subsequent FEL pulse irradiate a new sample by raster scanning of the solid membrane. Avoiding repeated irradiation of the same previously examined location helps ensure that data are collected from a fresh sample. In combination with a fast and accurate scanning system, silicon chips such as those described in Ref. [247] provide a high density of crystal wells on the chip and allow serial scanning of up to 100,000 crystal wells per hour [248, 249]. Such chips allow optical excitation as well as on-chip mixing for reaction triggering, making a wide variety of protein systems suitable for time-resolved studies [234].

4.4.2 Timing of pump and probe pulses. The X-ray pulses generated by X-ray FELs have excellent characteristics compared to those of third-generation synchrotrons. However, the shorter FEL pulses (which are advantageous in terms of time resolution) exhibit large fluctuations in intensity, arrival time, and energy due to the stochastic nature of the radiation [250]. For this reason, the jitter between the X-ray pulse and the optical laser pulse has to be corrected to improve the time resolution [251, 252].

To address this issue, X-ray/optical cross-correlators have been developed [142, 253–259] that measure the relative jitter of the arrival times of the FEL and laser pulses to allow correction of this jitter by subsequent data analysis [142, 260–262]. Such cross-correlation schemes may significantly improve the temporal resolution, but the method is applicable only to certain types of experiments.

To develop a generally applicable solution, an alternative strategy was employed. An optical timing system involving stabilized optical links was implemented [263], which allowed the development of an electron bunch arrival time monitor for cross-correlation with a timed optical reference [264]. More recently, the pump laser timing system with an all-electron RF system was upgraded to all-optical timing, which incorporated several time stabilization schemes [265]. These modifications significantly improved the stability and temporal resolution of the pump–probe experiments, which may eventually obviate the need for additional X-ray/optical arrival time measurements [266].

Another approach is to consider a setup with an X-ray probe with an X-ray pump using two FEL pulses [267–269]. This allows one to study the ultrafast dynamics associated with the excitation of core electrons and subsequent multiple ionization initiated by high-intensity X-ray radiation. Furthermore, the use of double FEL pulses allows spontaneous atomic fluctuations in condensed matter and plasmas to be studied with a high temporal resolution [270].

Consider two approaches to generating double FEL pulses. One is accelerator-based, while the other is X-ray optics-based. The first uses a simple and powerful method in which a magnetic chicane is placed between two undulators

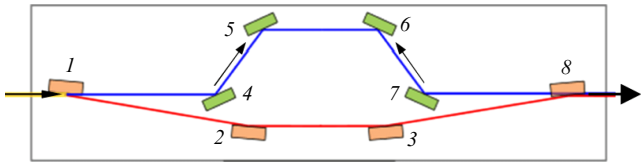

Figure 13. Schematic diagram of typical splitting and delay device: *1* — splitter, *2*, *3* — lower branch crystals (mirrors), *4*, *5*, *6*, *7* — upper branch crystals, *8* — mixer. Arrows along beam path of upper branch show how length of this path can be adjusted by moving crystals *5* and *6* [277].

[271–275]. Here, an FEL pulse is generated by an electron bunch in the first undulator, and then another pulse is produced by the same electron bunch in the second undulator. The time separation between the two FEL pulses is controlled by changing the deflection angle (i.e., path length) of the electron beam in the chicane [270].

Unfortunately, this method relies on special FEL operation modes and is not widely available to users. Moreover, due to the small deflection angle, it offers a limited range of available delays (typically from zero to several hundred fs) [269].

The second approach to double FEL pulse generation uses mirrors and single crystals in a quasi-noninvasive environment. It involves the division of the incoming FEL pulse into two parts by a beam splitter. The divided pulses travel along two different trajectories (upper and lower branches) (Fig. 13). By varying the path length of the upper branch, the arrival time difference (Δt) between the two pulses can be varied from 0 to 800 ps with an accuracy of several fs [276].

For the experimental implementation of this technique, which is called the split-and-delay technique, mirrors [278–281], multilayer structures [282], and Bragg crystals (e.g. [277, 283–286]) that encompass the regions of soft and hard X-ray radiation are used as optical elements.

There are several alternative splitting methods: wavelength splitting, wavefront splitting, and amplitude splitting.

The spectral bandwidth of the original X-ray beam exceeds the spectral reflection width of a single crystal. Part of the beam with photon energies falling within this band is reflected, and the rest of the beam passes through a beam splitter and is transmitted to the other branch. This method of wavelength splitting was used in Refs [270, 276, 287–289].

Wavelength splitting is convenient to use at large Bragg angles. For example, in Refs [285, 290], splitting and delay devices are described that use a diffraction angle of 90° (Fig. 14). The advantage of this optical geometry is that the time delay is created by moving the crystals C2, C3, C6, and C7 as a single unit in the perpendicular direction to the primary beam.

When splitting the wavefront, use is made of a crystal with polished edges: part of the primary beam passes over the edge of the beam splitter into one branch, and the other part of the beam satisfies the Bragg condition (or the condition of total external reflection of the X-rays) and is redirected into the other branch [277, 279–281, 291–293].

Figure 15 shows the optical configuration of the device illustrating the use of wavefront splitting to produce a pair of FEL pulses. Part of the primary beam below the highest point of the beam splitter (mirror M1) is reflected, and the part of the beam passing the beam splitter illuminates mirror M2. This simple design covers the energy range of

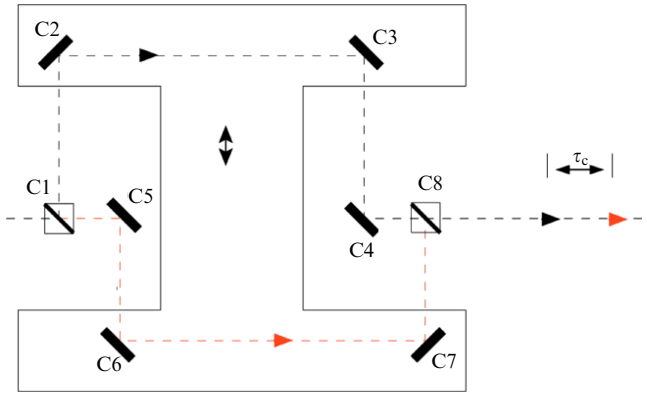

Figure 14. Schematic diagram of splitting and delay line with eight optical components. C1 is beam splitter, C2, C3, C4 are upper branch reflectors, C5, C6, C7 are lower branch reflectors, C8 is mixer, τ_c is time delay [285] (see text).

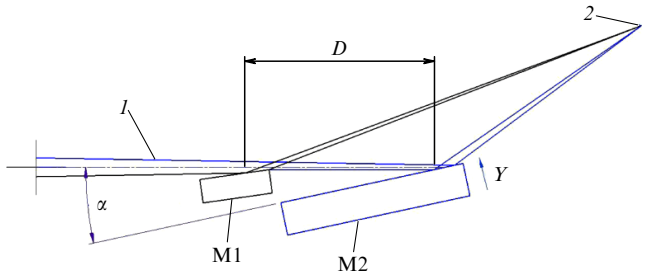

Figure 15. Optical diagram of splitting and delay device for focused XRs *1*, consisting of two mirrors: M1 is mirror that splits primary pulse into two and produces first pulse; M2 is mirror that produces second pulse, *2* is focus; distance D, angle of inclination α, and displacement Y of mirror M2 determine time delay [278].

250–1800 eV and provides a delay between two split pulses variable from 0 to 400 fs with a resolution of better than 100 as [278, 294, 295].

A conventional wavefront splitting line, although it provides double pulses with a high efficiency, suffers from the instability of crystal optics beam splitters and does not maintain sufficient mutual coherence between the two pulses [289]. The amplitude splitting approach can use a diffraction grating as a beam splitter, which generates a set of hard X-ray pulses with a high mutual coherence [296, 297].

The amplitude splitting approach was also used by the authors of Ref. [298]. They proposed a prototype of a splitting and delay device based on the Graeff–Bonse interferometer [299]. As shown in Fig. 16, sections M_I^T and M_{II}^T are cut at an angle of 12.5°. This tilt produces a delay time due to the change in the position of the beam reflected by these sections. Since the device is cut from a silicon monoblock, the time delay is produced by moving it perpendicular to the direction of propagation of the primary beam. Figure 16 shows two examples: no delay time (*1*) and finite delay time (*2*). The device can provide a delay time from 20 to 40 ps with a resolution of better than 26 fs.

In Refs [270, 276, 282, 289, 292, 300], crystals *2*, *3* of the lower branch (see Fig. 13) were replaced by monoblock double-arm reflectors (Fig. 17): since the directions of propagation of the incident and reflected beams coincide (the diffraction angle is zero), it is possible to significantly simplify the design of the device and its alignment.

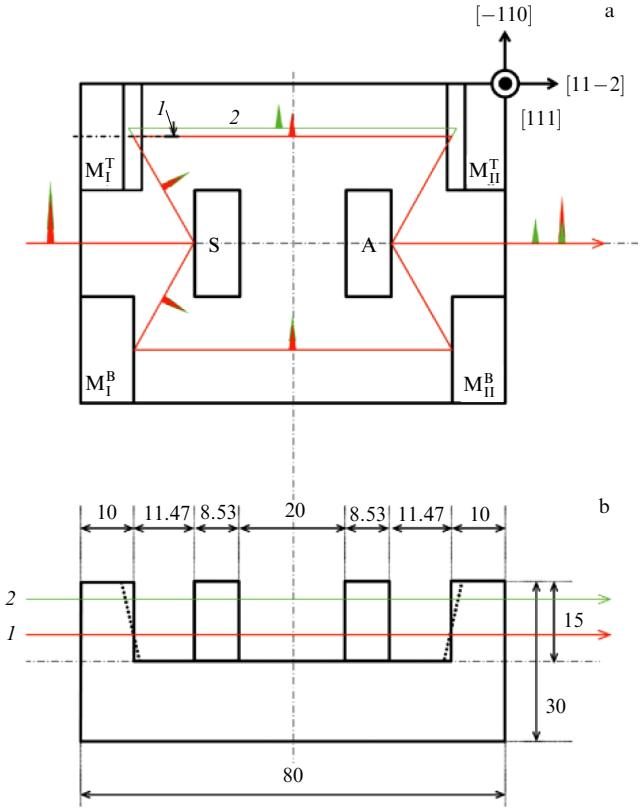

Figure 16. Schematic diagram of single-block splitter and delay device: (a) top view, (b) front view. S is splitter, A is mixer, M_I^T, M_{II}^T, M_I^B, and M_{II}^B are reflectors. Beam positions *1* and *2* correspond to absence or presence of time delay. FEL pulse energy was tuned to 7.46 keV ($\lambda = 1.662$ Å) or 14.92 keV ($\lambda = 0.831$ Å) (all dimensions in millimeters) [298] (see text).

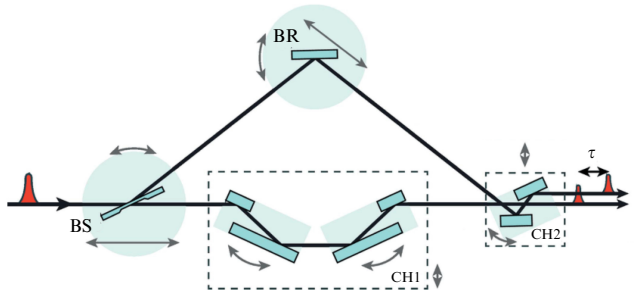

Figure 17. Concept of splitter and delay device. Arrows beside optical components indicate their main movements. BS is beam splitter, BR is reflector of upper branch, and CH1 is crystal system of lower branch with single-block double-arm reflectors. CH2 module changes directions of output beams; τ is delay [300].

4.4.3 Applications. *Protein Crystallography*. One of the most promising aspects of serial time-resolved X-ray crystallography is the ability to study the structural dynamics of proteins and other macromolecules in crystalline form without the reaction having to be cyclic. This is potentially transformative for the entire area and arises because diffraction data are collected from each microcrystal only once [219].

The first time-resolved experiment in serial protein crystallography was reported in Ref. [301] with time delays of 5 and 10 fs. However, the difference electron density maps needed to resolve the light-activated structure were not obtained. In 2014, the first difference electron density map from time-resolved serial X-ray crystallography data was generated in the investigation of photoactive PYP [302]. Since then, several pioneering studies have been carried out on different proteins such as myoglobin [303], bacteriorhodopsin [304], photosystem II [305–307], phytochrome [308], and dihydrofolate reductase [309], which showed that cyclic changes and noncyclic reactions can be followed using FEL facilities [24, 93, 310].

It is pertinent to note the studies conducted using the most modern European FEL facility, which, unlike other XFELs (X-ray Free Electron Lasers), can generate pulses in the MHz frequency range [311, 313], which can be successfully used in serial femtosecond crystallography to track different reaction stages in a single experiment.

In serial time-resolved X-ray crystallography, each diffraction image is a thin slice of reciprocal space, with the result that each measured reflection represents only a small fraction of the scattering coefficient. Furthermore, individual X-ray images can differ by more than 200% in intensity. In light of this, the determination of accurate structure factors calls for a high Bragg peak multiplicity, with a minimum of 50 recommended, which is in sharp contrast to conventional synchrotron crystallography [314, 315]. According to the authors of Ref. [310], the Cheetah program [316], developed specifically for the analysis of serial time-resolved X-ray crystallography data, can be used for background correction and match finding. The diffraction patterns can then be indexed and combined using the CrystFEL software package [317] and refined using the Phenix software package [318].

Radiography of solutions. Recent years have seen no less important progress in the field of time-resolved X-ray scattering [16, 310, 319].

Many important elementary chemical reactions occur on ultrafast time scales from tens of fs to ps, for instance, the formation and breaking of chemical bonds, isomerization, and charge transfer. The advent of FEL has made it possible to study the structural dynamics of such fast reactions in real time using serial time-resolved X-ray diffraction of solutions. For example, in Ref. [320], the bond formation of the trimeric gold complex $[Au(CN)_2^-]_3$ was studied in real time. Furthermore, linearly polarized photoexcitation was employed to analyze anisotropic scattering patterns measured from temporally oriented molecules of the trimeric gold complex using [321].

Serial time-resolved X-ray diffraction of solutions was shown to allow subpicosecond and subangstrom determination of the intramolecular structural dynamics of a solute [251, 322], detailed studies of solvent rearrangement and the dynamics around photoexcited reactants [323, 324], as well as the effect of solvent on the structure and dynamics of dissociation reactions [325].

Several investigations were performed on low-molecule systems in the solution phase to identify interesting ultrafast phenomena, for example, of the ultrafast solvation dynamics of an iron complex [326] and the nonequilibrium dynamics of intramolecular electron transfer in the bimetallic RuCo complex [327]. These results demonstrate the unique capability to resolve the ultrafast structural dynamics of chemical reactions in solution with subpicosecond time resolution and to elucidate the structural dynamics of the solute, solvent, and solvation cage [116].

X-ray spectroscopy. Ultrashort X-ray pulses of FEL facilities have opened the way for femtosecond time-scale spectroscopic experiments. This has allowed the study of local electronic and structural modifications occurring in transi-

tion metal compounds immediately after photoexcitation [328]. For example, Santomauro et al. performed an experimental study of the dynamics of photogenerated electron capture in TiO_2 [175]. Ultrafast local structural modification on the atomic scale was studied in tungsten trioxide (WO_3) [329, 330] and bismuth vanadate ($BiVO_4$) [330].

Using femtosecond wide-angle time-resolved X-ray scattering, an investigation was made of the photodissociation of diiodomethane (CH_2I_2) in solution [331], and the photoexcited state of hematite α-Fe_2O_3 was studied in [183]. Studies were also conducted on the bimetallic complex $[(CN)_5Fe^{II}CNRu^{III}(NH_3)_5]^-$ [332] and aqueous solutions of the complex $[Fe(III)(C_2O_4)_2]^{3-}$ [333].

Diffraction on polycrystals and nanoparticles. With the advent of FELs, ultrafast laser excitation, which gives rise to nonequilibrium states, opened up the possibility of studying thermal processes. The dynamics of laser-induced nonequilibrium thermal processes that lead to expansion/contraction of the crystalline structure was investigated using serial time-resolved X-ray diffraction [334–336].

The authors of Ref. [337] observed the effect of compression of thin films of polycrystalline palladium, which was caused by the surface skin layer heated by an optical pulse propagating through the film during the first tens of ps. After this, lattice expansion came to prevail, which was followed by a quasi-stationary state on a nanosecond time scale.

Polycrystalline thin films tend to have inhomogeneities associated with grain boundaries, dislocations, stacking faults, and point defects. Melting is believed to be initiated primarily on structural defects that contain atoms with lower coordination numbers, and hence with more dangling bonds than in bulk samples, which results in spatial nonuniformity of the electron-phonon interaction velocity. According to observations of the authors of Ref. [336], ultrafast melting of polycrystalline Au films occurs when an optical laser pulse is absorbed over the sample skin depth (12 nm for a wavelength of 400 nm) to produce a population of hot electrons. During this process, the hot electrons transfer their energy to the crystal lattice primarily through block boundaries, which results in nonuniform melting.

Nanoparticles exhibit interesting properties due to their size and morphology; for example, they can exhibit anomalously low thermal conductivity, because the phonon mean free path approaches the particle size. This plays an important role, for example, in the design of new thermoelectric devices. There is basic interest in studying photoinduced dynamics in nanoparticles and nanostructures, because this allows understanding their mechanical and thermal properties out of equilibrium and during phase transitions. Particularly interesting scenarios arise when nanoparticles undergo phase transitions, such as optical laser-induced melting. Theoretical data suggest that nanoparticles can undergo reversible inhomogeneous melting to form a core–shell structure. The formation of a liquid outer shell has been observed in static experiments, but had not been confirmed on a picosecond time scale until the appearance of Ref. [338]. It was also assumed that the liquid shell formation is reversible at temperatures below the melting point. Using the example of Au nanoparticles irradiated by short FEL pulses, it was shown in Ref. [338] that only their outer region is subject to melting, and that partial melting occurs nonuniformly with complete restoration of the morphology with each repeated pumping.

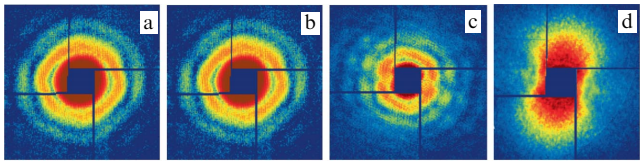

Figure 18. Diffraction patterns with time delays Δt obtained after irradiation of 100-nm-sized Au nanoparticles with single IR laser pulses with a time resolution of 10 ps using femtosecond FEL pulses. (a) Initial state, (b) $\Delta t = 40$ ps, (c) $\Delta t = 80$ ps, (d) $\Delta t = 140$ ps [339].

Figure 18 shows coherent diffraction patterns from single Au nanoparticles, which demonstrate anisotropic distortion of the diffraction pattern as the nanoparticles melt.

Photoelectron spectroscopy. Charge transfer and charge migration, in particular electron transfer, result in many important transformations in physics, chemistry, and biology. Charge transfer research often calls for determination of charge localization at a given time. When a molecule in its electronic ground state is photoexcited with electron transfer to an unoccupied orbital, complex reaction dynamics can occur, which often involves interactions between electronic and nuclear degrees of freedom and the formation of intermediate products. Since typical time scales for molecular vibrations are on the order of 10–100 fs, direct observation of atomic motion during a photochemical reaction has only become possible with the development of femtosecond laser technologies [340].

For instance, photoelectron spectroscopy of gas-phase molecules can provide information on ultrafast changes in molecular structure during chemical reactions, which is hardly obtainable by other methods. To prove the correctness of this statement, the authors of Ref. [341] performed photoionization experiments on 1-ethynyl-4-fluorobenzene (C_8H_5F) and 1,4-dibromobenzene ($C_6H_4Br_2$) polyatomic molecules adiabatically oriented by an optical pump laser.

Inner shell ionization or excitation is well suited for the initiation of intramolecular charge transfer, which can then be studied in a time-resolved experiment [342]. Notably, charge transfer investigations were performed on gas-phase molecules of iodomethane (CH_3I) [340, 343, 344] and fluoromethane (CH_3F) [344].

The development of FEL sources capable of generating two pulses with independently selectable wavelengths for pump and probe with a well-defined time spacing [272, 273] made it possible to relate the pump energy to a specific electronic excitation of a given element, for example, in magnetization dynamics studies in 3d-oxides of transition metals and rare earth metals and their compounds [345].

In Ref. [346], 10-fs-long X-ray pulses with intervals of 4.29 and 54 fs and energies of 690 eV for pumping and 683 eV for probing were used to study the fragmentation of XeF_2 molecules after absorption of X-rays. By choosing a pump pulse to excite the Xe atom and a probe pulse to excite the F atom, it is possible to observe transition states leading to the decay of the system into individual ions with femtosecond temporal resolution.

5. Conclusion

The method of pumping and X-ray probing has been used to advantage in recent decades to study a wide class of objects employing most of the known X-ray techniques, such as

topography, microscopy, crystal diffraction, small- and wide-angle scattering, and absorption spectroscopy. X-ray holography has been recently added to these methods [347]. However, despite recent achievements and promising prospects, much remains to be done and resolved in order to fully track fast processes in different systems of interest to researchers.

With the advent of FELs, many new operating modes have been proposed and tested to meet the modern requirements of the scientific community. Most of them improved the X-ray output characteristics and opened up new possibilities for FEL applications. However, there is still a set of creative ideas for further FEL development. These ideas aim to increase the output power [274], reducing the time jitter [252], shortening the pulse duration to the attosecond scale [348, 349], combining FELs and SR [350], reducing further the size of X-ray FELs [351], and equipping them with more advanced optical elements [352], including replacement of silicon elements with diamond ones.

As for FEL facilities, it is noteworthy that the rapid development of FEL applications and technologies has led to an increase in the global demand for access to FEL facilities, which are currently going over to high repetition rate operation (up to several MHz) using superconducting linear accelerators [350]. In this case, the time delay between two successive pulses is typically in the micro- and nanosecond range. This opens up the opportunity to explore the molecular dynamics range on submicrosecond time scales with the use of serial pulses to obtain multiple diffraction patterns from the same crystal.

An order of magnitude more experiments per year are typically conducted on SR facilities than on FEL ones, since there are many more synchrotron centers in the world. Therefore, the recent transfer of serial time-resolved crystallography technology to SR facilities may be of decisive importance for the further development of the pump and X-ray probe method [11].

One would also expect that a wider range of reactions could be studied if the method were used *in situ*/*operando mode* [251].

Due to rapid technological development in the generation of ultrahigh-intensity femtosecond and attosecond X-ray pulses, further improvements in the accuracy and reliability of time-resolved measurements can be foreseen, which will expand the range of applications of the pump and X-ray probe method in science and technology.

A high-intensity attosecond X-ray free-electron laser, which meets the requirements of attosecond science for studying quantum-mechanical electron motion in molecules and solids on a subfemtosecond time scale, is now available for attosecond pump and attosecond probe experiments in the soft X-ray region [353]. In the future, one would expect an extension of the method to the hard X-ray domain of FELs.

The work was performed within the framework of the state assignment of the National Research Center Kurchatov Institute.

References

1. Zewail A H *J. Phys. Chem. A* **104** 5660 (2000)
2. Davaasambuu J, Durand P, Techert S *J. Synchrotron Rad.* **11** 483 (2004)
3. Casaretto N et al. *Acta Cryst. B* **73** 696 (2017)
4. Fetisov G V *Sinkhrotronnoe Izluchenie. Metody Issledovaniya Struktury Veshchestv* (Synchrotron Radiation. Methods of Studying the Structure of Substances) (Moscow: Fizmatlit, 2007)
5. Neutze R, Moffat K *Curr. Opin. Struct. Biol.* **22** 651 (2012)
6. Tomov I V et al. *J. Phys. Chem. B* **103** 7081 (1999)
7. Schmidt M *Int. J. Mol. Sci.* **20** 1401 (2019)
8. Colletier J- P, Schirò G, Weik M, in *X-ray Free Electron Lasers: A Revolution in Structural Biology* (Eds S Boutet, P Fromme, M S Hunter) (Berlin: Springer Intern. Publ., 2018) p. 331, https://doi.org/10.1007/978-3-030-00551-1_11
9. Moffat K *Faraday Discuss.* **122** 65 (2003)
10. Moffat K *Chem. Rev.* **101** 1569 (2001)
11. Brändén G, Neutze R *Science* **373** eaba0954 (2021)
12. Malla T N, Schmidt M *Curr. Opin. Struct. Biol.* **74** 102376 (2022)
13. Ren Z et al. *Biochemistry* **40** 13788 (2001)
14. Kubelka J *Photochem. Photobiol. Sci.* **8** 499 (2009)
15. Thompson M C et al. *Nat. Chem.* **11** 1058 (2019)
16. Henry L et al. *Struct. Dyn.* **7** 054702 (2020)
17. Berntsson O, Terry A E, Plivelic T S *J. Synchrotron Rad.* **29** 555 (2022)
18. Schlichting I et al. *Science* **287** 1615 (2000)
19. Colletier J-P et al. *Proc. Natl. Acad. Sci. USA* **105** 11742 (2008)
20. Hekstra D R et al. *Nature* **540** 400 (2016)
21. Schmidt M *Adv. Condensed Matter Phys.* **2013** 167276 (2013)
22. Beyerlein K R et al. *IUCrJ* **4** 769 (2017)
23. Olmos J L (Jr.) et al. *BMC Boil.* **16** 59 (2018)
24. Pandey S, Poudyal I, Malla T N *Crystals* **10** 628 (2020)
25. Lorenc M et al. *Phys. Rev. Lett.* **103** 028301 (2009)
26. Baxter R H G et al. *Proc. Natl. Acad. Sci. USA* **101** 5982 (2004)
27. Poddar H et al. *FEBS J.* **289** 576 (2022)
28. Fetisov G V *Phys. Usp.* **63** 2 (2020); *Usp. Fiz. Nauk* **190** 2 (2020)
29. Henrich B et al. *Nucl. Instrum. Meth. Phys. Res. A* **607** 247 (2009)
30. Pangaud P et al. *Nucl. Instrum. Meth. Phys. Res. A* **571** 321 (2007)
31. Medjoubi K et al. *J. Synchrotron Rad.* **17** 486 (2010)
32. Dinapoli R et al. *Nucl. Instrum. Meth. Phys. Res. A* **650** 79 (2011)
33. Johnson I et al. *J. Synchrotron Rad.* **19** 1001 (2012)
34. Allé P et al. *Phys. Scr.* **91** 063001 (2016)
35. Wu Y, Takano H, Momose A *Proc. SPIE* **11113** 111130Z (2019)
36. Olbinado M P et al. *Appl. Phys. Express* **6** 096601 (2013)
37. Kamiński R, Nottingham G, Coppens P *J. Appl. Cryst.* **47** 1765 (2014)
38. Basuroy K et al. *Struct. Dyn.* **4** 024501 (2017)
39. Coppens P et al. *Acta Cryst. A* **61** 162 (2005)
40. Fullagar W K et al. *J. Synchrotron Rad.* **7** 229 (2000)
41. Gembicky M, Adachi S, Coppens P *J. Synchrotron Rad.* **14** 295 (2007)
42. Wulff M et al. *Faraday Discuss.* **122** 13 (2003)
43. Cammarata M et al. *Rev. Sci. Instrum.* **80** 015101 (2009)
44. Graber T et al. *J. Synchrotron Rad.* **18** 658 (2011)
45. Levantino M et al. *C. R. Physique* **22** 75 (2021)
46. Adachi S, Kim J, Ihee H, in *Advances in Lasers and Electro Optics* (Eds N Costa, A Cartaxo) (London: IntechOpen, 2010) p. 787, https://doi.org/10.5772/8658
47. Chergui M, Collet E *Chem. Rev.* **117** 11025 (2017)
48. Chollet M et al. *J. Synchrotron Rad.* **22** 503 (2015)
49. Ichiyanagi K et al. *J. Synchrotron Rad.* **16** 391 (2009)
50. Fukuyama Y et al. *Rev. Sci. Instrum.* **79** 045107 (2008)
51. Kjær K S et al. *Phys. Chem. Chem. Phys.* **15** 15003 (2013)
52. Yamamoto S, Matsuda I *J. Phys. Soc. Jpn.* **82** 021003 (2013)
53. Potemkin F V et al. *Rev. Sci. Instrum.* **92** 053101 (2021)
54. Marchenkov N et al. *Optics* **5** (1) 1 (2024)
55. Moffat K *Philos. Trans. R. Soc. A* **377** 20180243 (2019) https://doi.org/10.1098/rsta.2018.0243
56. Beaud P et al. *Phys. Rev. Lett.* **99** 174801 (2007)
57. Zholents A A, Zolotorev M S *Phys. Rev. Lett.* **76** 912 (1996)
58. Schoenlein R W et al. *Science* **287** 2237 (2000)
59. Maiuri M, Garavelli M, Cerullo G *J. Am. Chem. Soc.* **142** 3 (2020)
60. Khan S et al. *Phys. Rev. Lett.* **97** 074801 (2006)
61. Shimada M et al. *Jpn. J. Appl. Phys.* **46** 7939 (2007)
62. Heimann P A et al. *AIP Conf. Proc.* **879** 1195 (2007)
63. Evain C et al. *New J. Phys.* **14** 023003 (2012)
64. Stoll H et al. *Appl. Phys. Lett.* **84** 3328 (2004)
65. Fischer P et al. *J. Magn. Magn. Mater.* **310** 2689 (2007)

66. Bocklagel L et al. *Phys. Rev. B* **78** 180405 (2008)
67. Wessels P et al. *J. Phys. Conf. Ser.* **463** 012023 (2013)
68. Woo S et al. *Nat. Commun.* **8** 15573 (2017)
69. Chou K W et al. *J. Appl. Phys.* **99** 08F305 (2006)
70. Vansteenkiste A et al. *Phys. Rev. B* **77** 144420 (2008)
71. Vansteenkiste A et al. *Nature Phys.* **5** 332 (2009)
72. Rao S et al. *Sci. Rep.* **5** 10695 (2015)
73. Kirz J, Jacobsen C *J. Phys. Conf. Ser.* **186** 012001 (2009)
74. Lider V V *Phys. Usp.* **60** 187 (2017); *Usp. Fiz. Nauk* **187** 201 (2017)
75. Wessels P et al. *J. Phys. Conf. Ser.* **499** 012009 (2014)
76. Vogt U et al. *Opt. Lett.* **31** 1465 (2006)
77. Poudyal I et al., arXiv:2210.06243v3
78. Ren Z et al. *J. Synchrotron Rad.* **6** 891 (1999)
79. Stoddard B L *Curr. Opin. Struct. Biol.* **8** 612 (1998)
80. Bourgeois D et al. *Photochem. Photobiol. Sci.* **6** 1047 (2007)
81. Moffat K, Szebenyi D, Bilderback D *Science* **223** 1423 (1984)
82. Ihee H et al. *Proc. Natl. Acad. Sci. USA* **102** 7145 (2005)
83. Knapp J E et al. *Proc. Natl. Acad. Sci. USA* **103** 7649 (2006)
84. Šrajer V et al. *J. Synchrotron Rad.* **7** 236 (2000)
85. Coppens P, Fournier B *J. Synchrotron Rad.* **22** 280 (2015)
86. Coppens P et al. *J. Synchrotron Rad.* **16** 226 (2009)
87. Schotte F et al. *Proc. Natl. Acad. Sci. USA* **109** 19256 (2012)
88. Powell H R, Johnson O, Leslie A G W *Acta Cryst. D* **69** 1195 (2013)
89. Kabsch W *Acta Cryst. D* **66** (2) 125 (2010)
90. Duisenberg A J M *J. Appl. Cryst.* **25** 92 (1992)
91. Gevorkov Ya et al. *Acta Cryst. A* **76** 121 (2020)
92. Winn M D et al. *Acta Cryst. D* **67** 235 (2011)
93. Deresz K A et al. *Crystals* **11** 1345 (2021)
94. Kalinowski J A, Makal A, Coppens P *J. Appl. Cryst.* **44** 1182 (2011)
95. Kalinowski J A et al. *J. Synchrotron Rad.* **19** 637 (2012)
96. Yang X, Ren Z, Moffat K *Acta Cryst. D* **54** 367 (1998)
97. Schmidt M et al. *Biophys. J.* **84** 2112 (2003)
98. Makal A et al. *Acta Cryst. A* **67** 319 (2011)
99. Benedict J B et al. *Chem. Commun.* **47** 1704 (2011)
100. Jarzembska K N et al. *Inorg. Chem.* **53** 10594 (2014)
101. Coppens P et al. *Phys. Scr.* **91** 023003 (2016)
102. Trzop E et al. *Acta Cryst. A* **70** C776 (2014)
103. Schmidt M et al. *Proc. Natl. Acad. Sci. USA* **102** 11704 (2005)
104. Šrajer V et al. *Science* **274** 1726 (1996)
105. Bourgeois D et al. *Proc. Natl. Acad. Sci. USA* **103** 4924 (2006)
106. Schotte F et al. *Science* **300** 1944 (2003)
107. Hummer G, Schotte F, Anfinrud P A *Proc. Natl. Acad. Sci. USA* **101** 15330 (2004)
108. Jung Y O et al. *Nat. Chem.* **5** 212 (2013)
109. Makal A et al. *J. Phys. Chem. A* **116** 3359 (2012)
110. Aulchenko V M et al. *Phys. Usp.* **61** 515 (2018); *Usp. Fiz. Nauk* **188** 576 (2018)
111. Sharafutdinov M et al. *J. Synchrotron Rad.* **10** 384 (2003)
112. Rogachev A S et al. *Crystallogr. Rep.* **48** 466 (2003); *Kristallografiya* **48** 511 (2003)
113. Sharafutdinov M et al. *Nucl. Instrum. Meth. Phys. Res. A* **575** 149 (2007)
114. Boldyrev V V et al. *Dokl. Akad. Nauk SSSR* **259** 1127 (1981)
115. Aleksandrov V V et al. *Combust. Explos. Shock Waves* **19** 430 (1983); *Fizika goreniya i vzryva* **19** (4) 65 (1983)
116. Ki H et al. *Annu. Rev. Phys. Chem.* **68** 473 (2017)
117. Kim T K et al. *Chem. Phys. Chem.* **10** 1958 (2009)
118. Kim K H et al. *Struct. Dyn.* **1** 011301 (2014)
119. Kim T W et al. *Proc. Natl. Acad. Sci. USA* **117** 14996 (2020)
120. Svergun D, Barberato C, Koch M H J *J. Appl. Cryst.* **28** 768 (1995)
121. Schneidman-Duhovny D et al. *Biophys. J.* **105** 962 (2013)
122. Lee Y, Lee H, Ihee H *Chem. Phys. Rev.* **3** 041304 (2022)
123. Henry E R, Hofrichter J *Meth. Enzymol.* **210** 129 (1992)
124. Shlens J, arXiv:1404.1100
125. Hirai M et al. *J. Synchrotron Rad.* **9** 202 (2002)
126. Makowski L et al. *J. Mol. Biol.* **375** 529 (2008)
127. Cammarata M et al. *Nat. Methods* **5** 881 (2008)
128. Kim J G et al. *Acc. Chem. Res.* **48** 2200 (2015)
129. Lipfert J, Doniach S *Annu. Rev. Biophys.* **36** 307 (2007)
130. Makowski L *J. Struct. Funct. Genomics* **11** 9 (2010)
131. Rimmerman D et al. *J. Phys. Chem. Lett.* **8** 4413 (2017)
132. Rimmerman D et al. *Photochem. Photobiol. Sci.* **17** 874 (2018)
133. Rimmerman D et al. *J. Phys. Chem. B* **123** 2016 (2019)
134. Ravishankar H et al. *Sci. Adv.* **6** eaaz0981 (2020)
135. Josts I et al. *IUCrJ* **5** 667 (2018)
136. Berntsson O et al. *Structure* **25** 933 (2017)
137. Berntsson O et al. *Sci. Adv.* **5** eaaw1531 (2019)
138. Heyes D J et al. *Commun. Biol.* **2** 1 (2019)
139. Neutze R et al. *Phys. Rev. Lett.* **87** 195508 (2001)
140. Plech A et al. *Phys. Rev. Lett.* **92** 125505 (2004)
141. Ihee H et al. *Science* **309** 1223 (2005)
142. Harmand M et al. *Nat. Photon.* **7** 215 (2013)
143. Cho H S et al. *Proc. Natl. Acad. Sci. USA* **107** 7281 (2010)
144. Kim J et al. *J. Phys. Chem. Lett.* **2** 350 (2011)
145. Kim K H et al. *Chem. Commun.* **47** 289 (2011)
146. Kim T W et al. *J. Am. Chem. Soc.* **134** 3145 (2012)
147. Ramachandran P L et al. *J. Am. Chem. Soc.* **133** 9395 (2011)
148. Andersson M et al. *Structure* **17** 1265 (2009)
149. Westenhoff S et al. *Nat. Methods* **7** 775 (2010)
150. Korneev V N et al. *J. Surf. Investig.* **2** 872 (2008); Korneev V N et al. J. surf. Investig. 2872 (2008); *Poverkhnost'. Rentgen., Sinkhrotr. i Neitr. Issled.* (12) 61 (2008)
151. Tolochko B P et al. *Nucl. Instrum. Meth. Phys. Res. A* **467–468** 990 (2001)
152. Ten K A et al. *Fullerenes Nanotubes Carbon Nanostruct.* **20** 587 (2012)
153. Rubtsov I A et al. *J. Phys. Conf. Ser.* **1787** 012029 (2021)
154. Rubtsov I A *Sibirskii Fiz. Zh.* **17** 48 (2022)
155. Titov V M, Anisichkin V F, Mal'kov I Yu *Combust. Explos. Shock Waves* **25** 372 (1989); *Fizika goreniya i vzryva* **25** (3) 117 (1989)
156. Titov V M et al. *Diamond Relat. Mater.* **16** 2009 (2007)
157. Rubtsov I A et al. *J. Phys. Conf. Ser.* **774** 012071 (2016)
158. Rehr J J, Albers R C *Rev. Mod. Phys.* **72** 621 (2000)
159. Bressler Ch et al. *Science* **323** 489 (2009)
160. Volkov M et al. *Nature Phys.* **15** 1145 (2019)
161. Bressler C, Chergui M *Chem. Rev.* **104** 1781 (2004)
162. Lee J-W et al. *J. Synchrotron Rad.* **27** 953 (2020)
163. Bressler C, Abela R, Chergui M *Z. Kristallogr.* **223** 307 (2008)
164. Ahr B et al. *Phys. Chem. Chem. Phys.* **13** 5590 (2011)
165. Chergui M, Zewail A H *ChemPhysChem.* **10** 28 (2009)
166. Bressler C et al. *Nucl. Instrum. Meth. Phys. Res. A* **467–468** 1444 (2001)
167. Bressler C et al. *J. Chem. Phys.* **116** 2955 (2002)
168. Saes M et al. *Phys. Rev. Lett.* **90** 047403 (2003)
169. Gawelda W et al. *Phys. Scr.* **2005** (T115) 102 (2005)
170. Gawelda W et al. *Phys. Rev. Lett.* **98** 057401 (2007)
171. Sato T et al. *J. Synchrotron Rad.* **16** 110 (2009)
172. Johnson S L et al. *Phys. Rev. Lett.* **91** 157403 (2003)
173. Huse N et al. *J. Phys. Chem. Lett.* **2** 880 (2011)
174. Cavalleri A et al. *Phys. Rev. Lett.* **95** 067405 (2005)
175. Santomauro F G et al. *Sci. Rep.* **5** 14834 (2015)
176. Cho H et al. *Faraday Discuss.* **157** 463 (2012)
177. Rittmann-Frank M H et al. *Angew. Chem. Int. Ed.* **53** 5858 (2014)
178. Canton S E et al. *Faraday Discuss.* **185** 51 (2015)
179. Tromp M et al. *J. Phys. Chem. B* **117** 7381 (2013)
180. Wen H et al. *Sci. Rep.* **5** 15098 (2015)
181. Penfold T J et al. *Nat. Commun.* **9** 478 (2018)
182. Uemura Y et al. *Chem. Lett.* **43** 977 (2014)
183. Ismail A S M et al. *Phys. Chem. Chem. Phys.* **22** 2685 (2019)
184. Ishiguro N et al. *ACS Catal.* **2** 1319 (2012)
185. Baran T et al. *Electrochim. Acta* **207** 16 (2016)
186. Neppl S, Gessner O *J. Electron. Spectrosc. Relat. Phenom.* **200** 64 (2015)
187. Shavorskiy A et al. *AIP Conf. Proc.* **1525** 475 (2013)
188. Ogawa M et al. *Phys. Rev. B* **87** 235308 (2013)
189. Ogawa M et al. *Phys. Rev. B* **88** 165313 (2013)
190. Yukawa R et al. *Appl. Phys. Lett.* **105** 151602 (2014)
191. Ogawa M et al. *Rev. Sci. Instrum.* **83** 023109 (2012)
192. Loether B W et al. *Opt. Lett.* **41** 1977 (2016)
193. Jacques V L R et al. *Phys. Rev. Lett.* **117** 156401 (2016)
194. Lundh O et al. *Med. Phys.* **39** 3501 (2012)
195. Hädrich S et al. *J. Phys. B* **49** 172002 (2016)
196. Andreev A A, Platonov K Yu *Quantum Electron.* **46** 109 (2016); *Kvantovaya Elektron.* **46**109 (2016)
197. Mo M Z et al. *Rev. Sci. Instrum.* **84** 123106 (2013)
198. Mahieu B et al. *Nat. Commun.* **9** 3276 (2018)

199. Schoenlein R et al. *Philos. Trans. R. Soc. A* **377** 20180384 (2019)
200. Li J et al. *Nat. Commun.* **8** 186 (2017)
201. Attar A R et al. *Science* **356** 54 (2017)
202. Pertot Y et al. *Science* **355** 264 (2017)
203. Zinchenko K S et al. *Sci. Rep.* **13** 3059 (2023)
204. Weisshaupt J et al. *Nat. Photon.* **8** 927 (2014)
205. Zhavoronkov N et al. *Opt. Lett.* **30** 1737 (2005)
206. Silies M et al. *Appl. Phys. A* **96** 59 (2009)
207. Zamponi F et al. *Appl. Phys. A* **96** 51 (2009)
208. Bonvalet A et al. *Opt. Lett.* **31** 2753 (2006)
209. Zhao D et al. *Appl. Sci.* **12** 4723 (2022)
210. Er A O, Chen J, Rentzepis P M *J. Appl. Phys.* **112** 031101 (2012)
211. Chen J, Chen W-K, Rentzepis P M *J. Appl. Phys.* **109** 113522 (2011)
212. Li R et al., arXiv:1803.02873v1
213. Li R et al. *J. Chem. Phys.* **151** 124702 (2019)
214. v. Korff Schmising C et al. *Phys. Rev. Lett.* **98** 257601 (2007)
215. Bargheer M et al. *Science* **306** 1771 (2004)
216. Dorchies F et al. *Phys. Rev. Lett.* **107** 245006 (2011)
217. Leguay P M et al. *Phys. Rev. Lett.* **111** 245004 (2013)
218. Neutze R et al. *Nature* **406** 752 (2000)
219. Neutze R *Phil. Trans. R. Soc. B* **369** 20130318 (2014)
220. Moffat K *Phil. Trans. R. Soc. A* **377** 20180243 (2019)
221. Schulz E C et al. *Acta Cryst. D* **78** 14 (2022)
222. Schmidt M *Struct. Dyn.* **10** 010901 (2023)
223. Chapman H N et al. *Nature* **470** 73 (2011)
224. Carini G A et al. *J. Phys. Conf. Ser.* **493** 012011 (2014)
225. Blaj G et al. *J. Synchrotron Rad.* **22** 577 (2015)
226. van Driel T B et al. *J. Synchrotron. Rad.* **27** 608 (2020)
227. Mozzanica A et al. *J. Instrum.* **11** (2) C02047 (2016)
228. Allahgholi A et al. *J. Synchrotron Rad.* **26** (1) 74 (2019)
229. Cheng R K Y *Crystals* **10** 215 (2020)
230. Thompson M C, Yeates T O, Rodriguez J A *F1000Research* **9** 667 (2020)
231. DePonte D P et al. *J. Phys. D* **41** 195505 (2008)
232. Johansson L C et al. *Nat. Methods* **9** 263 (2012)
233. Weierstall U et al. *Nat. Commun.* **5** 3309 (2014)
234. Johansson L C et al. *Trends Biochem. Sci.* **42** 749 (2017)
235. Hejazian M et al. *RSC Adv.* **10** 15694 (2020)
236. Vakili M et al. *J. Appl. Cryst.* **56** 1038 (2023)
237. Lee J-H, Zatsepin N A, Kim K H *Bio Design* **6** (1) 15 (2018)
238. Wang D et al. *J. Synchrotron Rad.* **21** 1364 (2014)
239. Mafuné F et al. *Acta Cryst. D* **72** 520 (2016)
240. Roessler C G et al. *Structure* **24** 631 (2016)
241. Echelmeier A et al. *Nat. Commun.* **11** 4511 (2020)
242. Fuller F D et al. *Nat. Methods* **14** 443 (2017)
243. Awel S et al. *Opt. Express* **29** 34394 (2021)
244. Hunter M S et al. *Sci. Rep.* **4** 6026 (2014)
245. Mueller C et al. *Struct. Dyn.* **2** 054302 (2015)
246. Nam D et al. *J. Phys. B* **49** 034008 (2016)
247. Mehrabi P et al. *J. Synchrotron Rad.* **27** 360 (2020)
248. Ebrahim A et al. *Acta Cryst. D* **75** 151 (2019)
249. Ebrahim A et al. *IUCrJ* **6** 543 (2019)
250. van Driel T B et al. *Faraday Discuss.* **177** 443 (2015)
251. Choi E H et al. *Chem. Sci.* **13** 8457 (2022)
252. Diez M et al. *Sci. Rep.* **11** 3562 (2021)
253. Sato T et al. *Appl. Phys. Express* **8** 012702 (2015)
254. Hartmann N et al. *Nat. Photon.* **8** 706 (2014)
255. Bionta M R et al. *Rev. Sci. Instrum.* **85** 083116 (2014)
256. Krupin O et al. *Opt. Express* **20** 11396 (2012)
257. Gahl C et al. *Nat. Photon.* **2** 165 (2008)
258. Katayama T et al. *Struct. Dyn.* **3** 034301 (2016)
259. Katayama T et al. *J. Synchrotron Rad.* **25** 592 (2019)
260. Schorb S et al. *Appl. Phys. Lett.* **100** 121107 (2012)
261. Riedel R et al. *Nat. Commun.* **4** 1731 (2013)
262. Eckert S et al. *Appl. Phys. Lett.* **106** 061104 (2015)
263. Kim J et al. *Opt. Express* **32** 1044 (2007)
264. Löhl F et al. *Phys. Rev. Lett.* **104** 144801 (2010)
265. Schulz S et al. *Nat. Commun.* **6** 5938 (2015)
266. Savelyev E et al. *New J. Phys.* **19** 043009 (2017)
267. Roling S, Zacharias H, in *Synchrotron Light Sources and Free-Electron Lasers. Accelerator Physics, Instrumentation and Science Applications* (Eds E J Jaeschke et al.) (Cham: Springer, 2016) p. 891, https://doi.org/10.1007/978-3-319-14394-1_24
268. Roling S, Zacharias H, in *Synchrotron Light Sources and Free-Electron Lasers. Accelerator Physics, Instrumentation and Science Application* (Eds E J Jaeschke et al.) (Cham: Springer, 2020) p. 1057, https://doi.org/10.1007/978-3-030-23201-6_24
269. Mandal A et al. *Eur. Phys. J. Spec. Top.* **230** 4195 (2021)
270. Osaka T et al. *Opt. Express* **24** 9187 (2016)
271. Ding Y et al. *Phys. Rev. Lett.* **109** 254802 (2012)
272. Lutman A A et al. *Phys. Rev. Lett.* **110** 134801 (2013)
273. Hara T et al. *Nat. Commun.* **4** 2919 (2013)
274. Duris J et al. *Nat. Photon.* **14** 30 (2020)
275. Reiche S et al. *Proc. Natl. Acad. Sci. USA* **119** e2117906119 (2022)
276. Lu W et al. *AIP Conf. Proc.* **1741** 030010 (2016)
277. Xu Y et al. *Photonics* **9** (3) 136 (2022)
278. Castagna J C et al. *J. Phys. Conf. Ser.* **425** 152021 (2013)
279. Mitzner R et al. *Opt. Express* **16** 19909 (2008)
280. Simoncig A et al. *Photonics* **9** (5) 314 (2022)
281. Dreimann M et al. *J. Synchrotron Rad.* **30** 479 (2023)
282. Roling S et al. *Proc. SPIE* **9210** 92100B (2014)
283. Stetsko Yu P, Shvyd'ko Yu V, Stephenson G B *Appl. Phys. Lett.* **103** 173508 (2013)
284. Roseker W et al. *Opt. Lett.* **34** 1768 (2009)
285. Roseker W et al. *Sci. Rep.* **10** 5054 (2020)
286. Peters W K et al. *Opt. Express* **31** 31410 (2023)
287. Roseker W et al. *Proc. SPIE* **8504** 85040I (2012)
288. Osaka T et al. *Proc. SPIE* **9210** 921009 (2014)
289. Sun Y et al. *Phys. Rev. Research* **2** 023099 (2020)
290. Roseker W et al. *J. Synchrotron Rad.* **18** 481 (2011)
291. Roling S et al. *Proc. SPIE* **8778** 87781G (2013)
292. van Thor J J, Madsen A *Struct. Dyn.* **2** 014102 (2015)
293. Osaka T et al. *IUCrJ* **4** 728 (2017)
294. Murphy B F et al. *Proc. SPIE* **8504** 850409 (2012)
295. Berrah N et al. *Opt. Express* **24** 11768 (2016)
296. Opara N L et al. *Struct. Dyn.* **5** 054303 (2018)
297. Li H et al. *Phys. Rev. Research* **3** 043050 (2021)
298. Sakamoto J et al. *J. Synchrotron Rad.* **24** 95 (2017)
299. Graeff W, Bonse U *Z. Phys.* **27** 19 (1977)
300. Rysov R et al. *J. Synchrotron Rad.* **26** 1052 (2019)
301. Aquila A et al. *Opt. Express* **20** 2706 (2012)
302. Tenboer J et al. *Science* **346** 1242 (2014)
303. Barends T R M et al. *Science* **350** 445 (2015)
304. Nogly P et al. *Science* **361** eaat0094 (2018)
305. Kern J et al. *Science* **340** 491 (2013)
306. Kupitz C et al. *Nature* **513** 261 (2014)
307. Suga M et al. *Nature* **543** 131 (2017)
308. Claesson E et al. *eLife* **9** e53514 (2020)
309. Cao H, Skolnick J *Struct. Dyn.* **6** 024701 (2019)
310. Hekstra D R *Annu. Rev. Biophys.* **52** 255 (2023)
311. Wiedorn M O et al. *Nat. Commun.* **9** 4025 (2018)
312. Grünbein M L et al. *Nat. Commun.* **9** 3487 (2018)
313. Grünbein M L et al. *Phys. Rev. Research* **3** 013046 (2021)
314. Coe J et al. *Methods Enzymol.* **557** 459 (2015)
315. Stagno J R et al. *Nature* **541** 242 (2017)
316. Barty A et al. *J. Appl. Cryst.* **47** 1118 (2014)
317. White T A et al. *J. Appl. Cryst.* **45** 335 (2012)
318. Adams P D et al. *Acta Cryst. D* **58** 1948 (2002)
319. Lee S J et al. *Sci. Adv.* **8** eabm6278 (2022)
320. Kim K H et al. *Nature* **518** 385 (2015)
321. Kim J G et al. *J. Phys. B* **48** 244005 (2015)
322. Gaffney K J *Chem. Sci.* **12** 8010 (2021)
323. Biasin E et al. *Nat. Chem.* **13** 343 (2021)
324. Katayama T et al. *Chem. Sci.* **14** 2572 (2023)
325. Nimmrich A et al. *J. Am. Chem. Soc.* **145** 15754 (2023)
326. Haldrup K et al. *J. Phys. Chem. B* **120** 1158 (2016)
327. Canton S E et al. *Nat. Commun.* **6** 6359 (2015)
328. Fracchia M et al. *Surfaces* **1** 138 (2018)
329. Koide A et al. *Phys. Chem. Chem. Phys.* **22** 2615 (2020)
330. Uemura Y et al. *Appl. Sci.* **10** 7818 (2020)
331. Panman M R et al. *Phys. Rev. Lett.* **125** 226001 (2020)
332. Liekhus-Schmaltz C et al. *J. Phys. Chem. Lett.* **13** 378 (2022)
333. Ogi Y et al. *Struct. Dyn.* **2** 034901 (2015)
334. Milathianaki D et al. *Science* **342** 220 (2013)
335. Hartley N J et al. *Appl. Phys. Lett.* **110** 071905 (2017)
336. Assefa T A et al. *Sci. Adv.* **6** eaax2445 (2020)

337. Suzana A F et al. *Phys. Rev. B* **107** 214303 (2023)
338. Clark J N et al. *Proc. Natl. Acad. Sci. USA* **112** 7444 (2015)
339. Ihm Y et al. *Nat. Commun.* **10** 2411 (2019)
340. Braußе F et al. *Phys. Rev. A* **97** 043429 (2018)
341. Boll R et al. *Faraday Discuss.* **171** 57 (2014)
342. Rolles D *Adv. Phys. X* **8** 2132182 (2023)
343. Erk B et al. *Science* **345** 288 (2014)
344. Boll R et al. *Struct. Dyn.* **3** 043207 (2016)
345. Ferrari E et al. *Nat. Commun.* **13** 10343 (2016)
346. Picón A et al. *Nat. Commun.* **7** 11652 (2016)
347. Vassholz M et al. *Nat. Commun.* **12** 3468 (2021)
348. Xu X et al. *Phys. Rev. Accel. Beams* **27** 011301 (2024)
349. Guo Z et al. *Nat. Photon.* **18** 691 (2024); arXiv:2401.15250
350. Huang N et al. *The Innovation* **2** 100097 (2021)
351. Rosenzweig J B et al. *New J. Phys.* **22** 093067 (2020)
352. Anand V et al. *J. Phys. Photonics* **3** 024002 (2021) https://doi.org/10.1088/2515-7647/abd4ef
353. Kang H-S, Ko I S *Nat. Photon.* **14** 7 (2020)